NATURAL RESOURCES

ANALYTICAL DATA FROM THE MONROE 7.5-MINUTE QUADRANGLE, KING AND SNOHOMISH COUNTIES, WASHINGTON—SUPPLEMENT TO OPEN FILE REPORT 2011-1

by Joe D. Dragovich, Shannon A. Mahan,
Megan L. Anderson, James H. MacDonald Jr.,
Gregory R. Wessel, S. Andrew DuFrane,
Recep Cakir, Jeffrey D. Bowman,
and Heather A. Littke

WASHINGTON
DIVISION OF GEOLOGY
AND EARTH RESOURCES
Open File Report 2011-2
November 2011

This report has not been edited or reviewed for conformity with Division of Geology and Earth Resources standards or geologic nomenclature

WASHINGTON STATE DEPARTMENT OF
Natural Resources
Peter Goldmark - Commissioner of Public Lands

ANALYTICAL DATA FROM THE MONROE 7.5-MINUTE QUADRANGLE, KING AND SNOHOMISH COUNTIES, WASHINGTON—SUPPLEMENT TO OPEN FILE REPORT 2011-1

by Joe D. Dragovich, Shannon A. Mahan,
Megan L. Anderson, James H. MacDonald Jr.,
Gregory R. Wessel, S. Andrew DuFrane,
Recep Cakir, Jeffrey D. Bowman,
and Heather A. Littke

WASHINGTON
DIVISION OF GEOLOGY
AND EARTH RESOURCES
Open File Report 2011-2
November 2011

WASHINGTON STATE DEPARTMENT OF
Natural Resources
Peter Goldmark - Commissioner of Public Lands

WASHINGTON STATE DEPARTMENT OF NATURAL RESOURCES
Peter Goldmark—*Commissioner of Public Lands*

DIVISION OF GEOLOGY AND EARTH RESOURCES
David K. Norman—*State Geologist*
John P. Bromley—*Assistant State Geologist*

Washington Department of Natural Resources
Division of Geology and Earth Resources

Mailing Address:
MS 47007
Olympia, WA 98504-7007

Street Address:
Natural Resources Bldg, Rm 148
1111 Washington St SE
Olympia, WA 98501

Phone: 360-902-1450
Fax: 360-902-1785
E-mail: geology@dnr.wa.gov
Website: http://www.dnr.wa.gov/ResearchScience/GeologyEarthSciences/Pages/Home.aspx

Publications List:
http://www.dnr.wa.gov/ResearchScience/Topics/GeologyPublicationsLibrary/Pages/pubs.aspx

Washington Geology Library Catalog:
http://www.dnr.wa.gov/ResearchScience/Topics/GeologyPublicationsLibrary/Pages/washbib.aspx

Washington State Geologic Information Portal:
http://www.dnr.wa.gov/ResearchScience/Topics/GeosciencesData/Pages/geology_portal.aspx

Suggested Citation: Dragovich, J. D.; Mahan, S. A.; Anderson, M. L.; MacDonald, J. H., Jr.; Wessel, G. R.; DuFrane, S. A.; Cakir, Recep; Bowman, J. D.; Littke, H. A., 2011, Analytical data from the Monroe 7.5-minute quadrangle, King and Snohomish Counties, Washington—Supplement to Open File Report 2011-1: Washington Division of Geology and Earth Resources Open File Report 2011-2, 58 p., 2 plates, 2 Microsoft Excel files.

Published in the United States of America

Contents

Figures

Tables

Analytical data from the Monroe 7.5-minute quadrangle, King and Snohomish Counties, Washington—Supplement to Open File Report 2011-1

by Joe D. Dragovich[1], Shannon A. Mahan[2], Megan L. Anderson[3], James H. MacDonald Jr.[4], Gregory R. Wessel[5], S. Andrew DuFrane[6], Recep Cakir[1], Jeffrey D. Bowman[1], and Heather A. Littke[1]

Geochemical Laboratory Analysts: Laureen C. Wagoner[7], Richard M. Conrey[7], and Charles M. Knaack[7]

[1] Washington Division of Geology and Earth Resources
MS 47007
Olympia, WA 98504-7007

[2] U.S. Geological Survey
Box 25046 MS 974
Denver Federal Center
Denver, CO 80225-5046

[3] Colorado College
Department of Geology
14 E Cache La Poudre St
Colorado Springs, CO 80903

[4] Florida Gulf Coast University
Department of Marine and Ecological Science
Fort Myers, FL 33965

[5] King County Department of Development and Environmental Services
900 Oakesdale Ave SW
Renton, WA 98057

[6] University of Alberta
Department of Earth and Atmospheric Sciences
1-26 Earth Sciences Building
Edmonton, Canada T6G 2E3

[7] Washington State University
School of Earth and Environmental Sciences
GeoAnalytical Laboratory
PO Box 642812
Pullman, WA 99164-2812

INTRODUCTION

Geologic mapping of the Monroe quadrangle is part of our broader effort to provide detailed geologic map information in the Snoqualmie valley area (Dragovich, 2007; Dragovich and Walsh, 2008; Dragovich and others, 2007, 2009a,b,c, 2010a,b). The reader is urged to examine the following data and analyses in conjunction with the geologic map of the Monroe 7.5-minute quadrangle by Dragovich and others (2011). The Monroe quadrangle document provides the geologic overview, geologic rock unit list, and unit symbology as well as the locations of some of the sites mentioned herein, including the locations of the IRSL and quartz OSL age sites, radiocarbon age sites, and some of the neotectonic and liquefaction sites. Several electronic appendices, tables, and figures accompany this report as outlined in Table 1 below. During this study, we discovered that Pleistocene nonglacial units in the northern part of the map area are ancient Skykomish River alluvium, which has a provenance very similar to the ancient SP alluvium. 'SP' below refers to ancient and modern alluvium with a Skykomish and Snoqualmie provenance.

See Dragovich and others (2011) for geologic symbols for the Monroe quadrangle bedrock geologic units cited below. For example, Eva_p is the symbol for the Eocene andesite flow from the volcanic rocks of Mount Persis of Tabor and others (1993). To aid our geographic descriptions, we informally name the uplands covering the southeastern part of the Monroe 7.5-minute quadrangle the 'southeast highlands' (SE highlands)—an extensive rocky upland from 'High Rock' on the northwest to Cherry Creek on the

southeast. Also, the finger-like upland north of the Skykomish River, southeast of Woods Creek, and surrounding age sites OW-8 and OW-5 is informally named 'Cougar Ridge' by Dragovich and others (2011). IRSL and OSL refer to the geochronologic methods Infrared Stimulated Luminescence (ages determined on feldspars) and Optically Stimulated Luminescence (ages determined on quartz), respectively. The southern Whidbey Island fault zone (SWIF) is a continuation of the correlative Rattlesnake Mountain fault zone (RMFZ).

Table 1. Location and brief description of appendices, tables, plates, or figures cited in this report.

Data	File name (attachments)	Notes
Appendix 1	See page 26	Radiocarbon ages in and near the Monroe 7.5-minute quadrangle
Appendix 2	See page 29 and a2_geochemical_data_monroe.xls	Geochemical data, petrography, and sample information; note the spreadsheet contains several tabs; see also Appendices 3–4
Appendix 3	See page 30	Geochemical sample site locations in the Monroe 7.5-minute quadrangle; see also location descriptions and other sample notes provided in Appendix 2; note spreadsheet contains multiple tabs
Appendix 4	See page 31	Additional geochemical plots; see also Figures 1A–1D
Appendix 5	See page 38 and a5_u_pb_geochronology_monroe.xls	Single zircon U-Pb data, plots, and sample information; note spreadsheet contains multiple tabs
Appendix 6	See page 39	Geophysical map (gravity and total magnetic field) of the Monroe 7.5-minute quadrangle, expanded version of geophysical cross section B of Dragovich and others (2011), and table of measured rock physical properties. Compare to geophysical illustrations (Figs. 1 and 2) on map sheet of Dragovich and others (2011)
Appendix 7	See page 42	Selected outcrop photos of deformational and liquefaction features in Quaternary deposits and rocks in the Monroe 7.5-minute quadrangle
Plate 1	p1_hypocenters_monroe.pdf	Hypocenters in and around the Monroe 7.5-minute quadrangle
Plate 2	p1_hypocenters_duvall.pdf	Hypocenters for the Duvall earthquake swarm; southeasternmost and southwesternmost parts of the Monroe and Sultan 7.5-minute quadrangles, respectively
Figure 1A–D	Embedded in this document	Geochemical plots; see Appendix 4 for additional plots
Figure 2A–C	Embedded in this document	Earthquake focal mechanism ternary diagram and hypocenter cross sections for the Duvall earthquake swarm in the southeastern and southwestern parts of the Monroe and Sultan 7.5-minute quadrangles, respectively
Table 2	See page 5	IRSL and OSL age data table for the Olympia beds, Whidbey Formation, and Hamm Creek formation samples in the Monroe 7.5-minute quadrangle
Table 3	See page 7	Major Quaternary provenances for glacial and nonglacial deposits in the Snoqualmie valley, including the Monroe 7.5-minute quadrangle

RADIOCARBON GEOCHRONOLOGY

Details about the new radiocarbon ages cited in Dragovich and others (2011) are provided in Appendix 1. For a more regional perspective on the Monroe and nearby areas, see radiocarbon ages in Dragovich and others (2007, 2009a,b,c, 2010a,b), Sherrod and others (2008), and Booth (1990), and references cited therein. These ages, combined with stratigraphic and sand compositional information, demonstrate that unit Qc_{ol} as exposed within southeast Cougar Ridge is similar to unit Qc_{ol} on Union Hill and easternmost Redmond Ridge, directly southwest of the current study area (Dragovich and others, 2010a,b, 2011). In all three cases, the thin (~0–50 ft [0–15 m] thick) nonglacial deposits correlate with the local provenance (LP) Olympia beds. (See LP in Table 3.) 'Infinite' radiocarbon ages cited in Appendix 1 are derived from organic materials that are older than the limit of the radiocarbon dating method (~44,000 yrs B.P. or 44 ka). Infinite ages obtained from other pre-Fraser SP sediments (unit Qc_{pf}) could be Olympia beds or older SP nonglacial units. (See SP in Table 3.) Our new IRSL and OSL ages (described below) show that at least some of the 'infinite' age sediments are Olympia beds, the Whidbey Formation, or the Hamm Creek formation of Troost and others (2005). Photos of some of the radiocarbon sample sites are provided in Appendix 7.

INFRARED STIMULATED LUMINESCENCE AND OPTICALLY STIMULATED LUMINESCENCE AGES FOR PLEISTOCENE NONGLACIAL BEDS

Methodology

GENERAL CONCEPTS OF LUMINESCENCE DATING

Most minerals react to ionizing radiation by essentially gaining energy at the electron level, which accumulates through time if that energy is not released (as light) by some outside stimuli (sunlight or intense heat over 200°C). Thus, sediment grains can record their exposure history to ionizing radiation, which can then be 'read' in the laboratory and used as a clock. This procedure is referred to as luminescence geochronology, the goal of which is to establish the timing of the burial of mineral grains in sedimentary deposits. Luminescence dating is based on solid-state dosimetric properties of natural mineral grains. Minerals react to ionizing radiation, which is generated by radioactive isotopes found in minor quantities in most terrestrial sediments and by cosmic radiation. Specifically, ionizing radiation creates charge pairs/carriers (e-, h+) in mineral crystals. The charge carriers are mobile within the crystals, but can become localized, or trapped, at lattice defects and held there over geologically significant time scales. Over time, the number of segregated, or trapped, charge carriers builds up in a way that can be described by a saturating exponential function. If the mineral grains were transported at night, in turbid fluvial conditions, or were generally considered to be deposited in massive, sudden discharge events (that is, debris flows, colluvium, etc.), luminescence dating may produce depositional ages that are too old because the luminescence clock was not reset to 'zero' prior to burial. Exposure to heat, light, or high pressures can release charge carriers from trapping sites (detrapping) and permit recombination, during which light is emitted from the mineral grains. This detrapping resets the system within the mineral grains. In terrestrial environments, exposure to sunlight during sediment transport resets the clock and it is also why a luminescence age is considered a burial age. In the laboratory, sediment is stimulated to emit light, which is measured. The sediment is stimulated by exposure to light of specific wavelengths (optically stimulated luminescence, OSL) or heat (thermoluminescence, TL) in a prescribed manner. The intensity of emitted light measured in the laboratory is proportional to the trapped charge population, which is proportional to the total absorbed radiation dose (D_e) that the sedimentary deposit experienced, and that relation is proportional to the time elapsed since burial (Duller, 2008). The simplest form of the OSL age equation is:

$$t_{OSL} = \frac{D_e}{D'}$$

where
t_{OSL} = age
D_e = total absorbed radiation dose,
D' = natural environmental dose rate.

A dose rate model was constructed that assumed moisture contents of ~60% of full saturation (that is, 26% of a possible 44%). This simple model should account for seasonal moisture variations, water content, and dose rate analysis as described by Mahan and others (2007), using methods modified from Aitken (1985), Murray and others (1987), and Snyder and Duval (2003).

SAMPLE COLLECTION

Luminescence samples were collected from freshly cleaned natural exposures for further processing. At least 50 cm of sediment was removed from the face of each exposure before sampling to minimize the possibility of bleaching of the outer layers of the sediment by modern sunlight. Opaque plastic tubes ~20 cm long were hammered perpendicularly into the exposed vertical faces to extract the sediment samples. The tubes were sealed and placed in light-proof photographic bags until the initial processing within a darkroom lab. All samples were processed at the USGS Luminescence Dating Laboratory in Denver, Colorado.

DETERMINING THE EQUIVALENT DOSE (D_E)

At least 5 cm of sediment was removed from both ends of the sampling tube under 'safe light' (sodium vapor lighting) conditions in the luminescence laboratory. The ends and the middle portion of the samples were dried in an oven at 30°C. The entire sample was leached in 4M HCl (10% HCl) for 24 hours, 30%

H_2O_2 for 24 hours, and 10% HF for 20 minutes. If no coarser sized grains remained (<170 mesh or 90 microns), the finer silt-size grains were used for IRSL dating. This type of luminescence stimulates only the feldspars even if those grains are in a polymineral mix.

IRSL was done on a polymineralic fine silt fraction (4–11 μm). The silt was preheated using a long, slow temperature of 124°C for 64 hours. IRSL analyses were performed on a Daybreak 1100 luminescence reader with Schott BG-39 filters coupled to an EMI 9635 QA photomultiplier tube. The silt was dated using the total-bleach multiple-aliquot additive-dose (MAAD) method (Singhvi and others, 1982; Richardson and others, 1997; Forman and Pierson, 2002). A minimum of two analyses per IRSL sample by MAAD methods was performed. Anomalous fading tests on the stability of the luminescence signal indicated little to no signal instability (recording ratios of 0.91 to 1.00 for a fade ratio of only 1 to 2 percent). Growth curve data were fit to an exponential trend. All samples were analyzed using continuous wave (CW-OSL) stimulation. The sample size for the silt-sized particles was on the order of many thousands of grains (but no actual count was attempted), covering the entire disc surface.

Quartz OSL was determined using an automated Risø TL/luminescence-DA-15 system for SAR analyses and CW-OSL was used. Single aliquot regeneration (SAR) protocols (Murray and Wintle, 2003; Wintle and Murray, 2006) were used in optical dating of fine-grained quartz separates. The natural and regenerated signals were bright and never close to background or 'dim'. The luminescence emissions for all of the quartz samples showed a slight mixed dominance of either a slow or medium component instead of the fast component on some discs (Murray and Wintle, 2003); often one signal or the other would appear on differing aliquots of the same sample when CW-OSL was employed. These discs were ultimately discarded before the final equivalent dose was calculated, but this discrepancy should be noted. The emissions had a >95% diminution of luminescence after four seconds of excitation with blue light. The majority of the discs showed clear access from the fast component of quartz OSL. All SAR emissions were integrated over the first 0.8 seconds of stimulation out of 40 seconds of measurement, with background based on emissions for the last 35 to 40 seconds of interval.

DETERMINING THE DOSE RATE (D_R)

Most ionizing radiation in the sediment is from the decay of isotopes in the uranium and thorium decay chains and the radioactive potassium-40 element. The dose rate was obtained by elemental data analyses. The concentrations of K, U, Th, and Rb were determined using gamma spectrometry following the procedures described in Snyder and Duval (2003). The bulk samples were dried, homogenized by gentle disaggregation, weighed, sealed in plastic planchets having a diameter of 15.2 cm by 3.8 cm (some modification from Murray and others, 1987), and then immediately placed in a low-resolution NaI detector gamma-ray spectrometer at the USGS Gamma Spectrometry Lab in Denver for ~8.5 hours. Samples were then stored for a minimum of 21 days to allow radon to achieve radioactive equilibrium, and the measurements were repeated. The fraction of radon emanation was estimated from the difference of these two spectrometer measurements. A sealed/unsealed ratio of <1.10 is not considered to represent significant radon escape under laboratory conditions. These count rates are accurate for calculating dose rates. Alpha and beta contributions to the dose rate were corrected for grain-size attenuation (Aitken, 1985). The alpha efficiency for the silt-sized samples was determined by comparing MAAD-alpha source exposed and MAAD-beta source exposed curves, using approaches in Aitken (1985). Measured elemental concentrations, associated dose rates, and cosmic ray contributions are presented in Table 2. Cosmic-ray dose rate data was estimated for each sample as a function of depth, elevation above sea level, and geomagnetic latitude (Prescott and Hutton, 1994).

Sample Site Descriptions and Results

Luminescence ages for sediment samples are presented in Table 2 and, along with the Pleistocene nonglacial character of the sediments, are evidence that the sampled strata are correlative with the Olympia beds, Whidbey Formation, or the Hamm Creek formation. (See units Qc_o, Qc_{ws}, Qc_h, in Dragovich and others [2011], including the geologic unit references and other information.) Petrographic and geochemical examination of nonglacial sands from each site, combined with deposit stratigraphy, show that each of the samples are monocrystalline quartz–rich ancient Snoqualmie or Skykomish alluvium with a strong Cascade batholith provenance. (See SP in Table 3.) We also obtained radiocarbon dating and geochemical analysis samples at most of the luminescence sample sites (Appendices 1, 3, and 4). Photos of some of the luminescence sample sites are provided in Appendix 7. The luminescence ages obtained for samples

corroborate our independent field, petrographic, and geochemical interpretation that these deposits are nonglacial in origin and thus deposited between glacial episodes as ancient alluvium.

Table 2. IRSL and quartz OSL data and ages from the Monroe quadrangle. Table provides elemental concentrations, cosmic and total dose rates, equivalent doses, and ages from IRSL (fine-grained feldspars) and quartz OSL. Sample descriptions are generalized; more detailed descriptions are provided above or in Dragovich and others (2011). Samples are located on the map sheet of Dragovich and others (2011). Reported to one sigma, as are ages. K, % potassium; Gy, Gray (unit of absorbed radiation); ka, 1000 yrs.

Sample information	Water content (%)[a]	K (%)[b]	U (ppm)[b]	Th (ppm)[b]	Cosmic dose[c] additions (Gy/ka)	Total dose rate (Gy/ka)	Equivalent dose (Gy)	n[d]	Age (ka)[e]
10-24A (Lewis Street Park, fine-grained sand)	12 (44)	0.92 ± 0.02	0.91 ± 0.06	2.85 ± 0.10	0.12 ± 0.01	1.17 ± 0.02	59.1 ± 3.96	20 (24)	50.5 ± 3.53
10-24B (N High Rock Rd, silty clay)	25 (75)	1.07 ± 0.02	1.63 ± 0.06	3.79 ± 0.09	0.13 ± 0.01	1.79 ± 0.03[f]	313 ± 5.00[f]	–	233 ± 10.9[f]
10-24C (Ben Howard Rd, sand)	11 (46)	0.80 ± 0.02	1.07 ± 0.05	2.61 ± 0.08	0.08 ± 0.01	1.03 ± 0.02	>182	19 (24)	>155
10-24D (260 Ave SE, sand)	12 (50)	1.21 ± 0.02	1.09 ± 0.06	3.10 ± 0.09	0.11 ± 0.01	1.37 ± 0.02	70.8 ± 5.19	20 (25)	51.1 ± 3.84
10-24E (Woods Creek Rd, silt)	13 (46)	1.03 ± 0.02	1.01 ± 0.05	2.33 ± 0.0	0.11 ± 0.01	1.64 ± 0.03[f]	202 ± 5.86[f]	–	123 ± 8.24[f]
10-25A (Cadman Quarry, sand)	3 (29)	0.92 ± 0.02	0.77 ± 0.07	2.31 ± 0.08	0.06 ± 0.01	1.13 ± 0.02	114 ± 4.9	26 (30)	101 ± 4.47
10-25B (Cadman Quarry, sand)	2 (29)	0.96 ± 0.02	0.74 ± 0.07	2.45 ± 0.09	0.06 ± 0.01	1.13 ± 0.03	121 ± 11.0	22 (24)	107 ± 9.87

[a] Field moisture, with figures in parentheses indicating the complete sample saturation %. Ages calculated using approximately 60% of saturation values, except WA-10-196 at 90% of saturation.

[b] Analyses obtained using laboratory gamma spectrometry (high resolution Ge detector).

[c] Cosmic doses and attenuation with depth were calculated using the methods of Prescott and Hutton (1994). (See text for details.) Total dose rate is measured using field moisture.

[d] Number of replicated equivalent dose (De) estimates used to calculate the mean. Figures in parentheses indicate total number of measurements made including failed runs with unusable data.

[e] Dose rate and age for fine-grained 180-90 microns quartz sand. Linear + exponential fit used on equivalent dose, with single aliquot regeneration.

[f] Lab used fine silt grains (5–10 micron size), data fit to an exponential regression and obtained as infrared stimulated luminescence on feldspar by multiple aliquot additive dose. Feldspar from fine grains of 4 to 11 micron polymineral silt. Exponential fit used for equivalent dose, multiple aliquot additive dose. Fade tests indicate no correction.

OLYMPIA BEDS

Sample 24A was obtained from an outcrop located at the intersection of Woods Creek and the Skykomish River (photo on p. 45). This river cutbank exposes a 20-ft-high and 30-ft-wide exposure of dense, stratified sands and silts. The deposits are intensively liquefied and contain rootless folds of silt beds surrounded by thicker beds of sand. Geographic position and distinct sand composition indicate that this is ancient Skykomish River alluvium. *Sample 24D* (photo on p. 47) was obtained from a 50-ft-high and 100-ft-wide partially vegetated roadcut along Ben Howard Road in the northern part of the SE highlands. This ancient alluvium coarsens upwards from stratified silt, silty sand, and sand to pebble gravel and contains low amplitude crossbeds. Most sands have an SP provenance as further discussed in Dragovich and others (2011).

WHIDBEY FORMATION

Samples 25A and 25B were obtained from nonglacial crossbedded sands and pebbly sands in the Cadman mine (elevation 403 ft)(photo on p. 48). These sand samples were extracted from a ~10-to-30 ft-high active mining face. This subvertical working face exposes ancient alluvium of the Whidbey Formation, is overlain by probable Vashon advance outwash, and is capped by a layer of Vashon till. Petrographic and geochemical examination of the sands shows that they vary from distinct Snoqualmie River ancient alluvium to sands with a more mixed provenance, likely as a result of local erosion during fluvial deposition. See Appendix 1 for the infinite radiocarbon age from this site. *Sample 24E* was obtained from a 10-ft-high and 30-ft-wide roadcut along a private driveway. This partially vegetated cutbank exposes dense micaceous fine sand, silty fine sand, and silt with discontinuous bedding as a result of liquefaction; mostly well stratified and very thickly bedded with the orangish cast typical of ancient SP alluvium. Like previous OSL samples, the sands are monocrystalline-quartz-rich (~20%) with significant but lesser hornblende and potassium feldspar and have a strong Cascade batholith provenance (Table 3).

HAMM CREEK FORMATION

Samples 24B (photo on p. 45) and *24C* are both from outcroppings of dense ancient alluvium. Exposures show numerous intense liquefaction features. Sample 24B is from a North High Rock Road cut-slope that exposes laminated to thinly bedded silt and silty fine sand. The outcrop is ~10 ft high and ~10 ft wide and located ~30 ft above the road. Sample 24C is from a large road cut above Ben Howard Road that exposes dense fine sands and silty fine sands that are typical ancient alluvium containing scattered lenticular beds of gravels. The sample was taken from ~20 ft above the road.

SAND POINT-COUNT DATA—SEDIMENTARY PROVENANCES AND INVERTED BASINS

Dragovich (2007) and Dragovich and others (2009a,b, 2010a,b) supply sand point-count data for various Quaternary geologic units including Holocene Snoqualmie River alluvium, Vashon glacial units, Olympia beds, Whidbey Formation, and Possession glacial outwash for the Fall City, Snoqualmie, and Carnation quadrangles. Provenances are defined by compositional data derived from sand point-count data, general petrographic observations, and sand geochemistry, as well as field data and observations. During this study, we visually estimated the percentages of various grain populations for 41 mounted sand thin sections from various Quaternary geologic units sampled in the Monroe quadrangle. We further examined the geochemistry of these provenances during this study as discussed below. As shown in Table 3, Quaternary strata in the Snoqualmie valley area are assigned to four major sedimentary provenances: (1) nonglacial Snoqualmie River southeastern source (SP), (2) nonglacial local eastern source (LP), (3) nonglacial Puget Group northern source (PG), and (4) glacial mixed northern source (GP) (Dragovich, 2007; Dragovich and others, 2009a,b,c, 2010a,b, 2011). Modern Snoqualmie River alluvium (unit Qa) is modally similar to ancient Snoqualmie River alluvium such as the Olympia beds (unit Qc_o), as well as the Whidbey Formation (unit Qc_{ws}), and these units have a distinct Snoqualmie River SP provenance. Additionally, Dragovich and others (2011) correlated some ancient SP with the Hamm Creek formation. They also surmised in the field and confirmed petrographically, geochemically, and geochronologically that most Pleistocene nonglacial units in the northern part of the Monroe quadrangle are ancient Skykomish River alluvium; and, they have a provenance very similar to the ancient and modern Snoqualmie alluvium. SP for both the Snoqualmie and Skykomish basins have a distinct granodiorite to granite batholith provenance with significant monocrystalline quartz (~10–20%), plagioclase, lesser but significant granitic lithic clasts, potassium feldspar, hornblende, and mica. Some ancient alluvium might have been deposited in a structural basin and (or) uplifted by later faulting as suggested by (1) anomalous thickness, (2) tilting, (3) folding, and (or) (4) elevation of the SP strata. For example, it is likely that thick SP stratigraphic sections represent ‘inverted basins’ resulting from strike-slip or reverse faulting within the SWIF (Dragovich and others, 2009a,b; 2010a,b). In this model, Dragovich and others (2010a,b) hypothesized that the thick SP alluvium formed in a transtensional basin within a broad active fault zone. The basin was inverted when the SP sediments underwent uplift and folding during a later (on-going?) transpressional episode. Furthermore, we suspect uplift or tilting of ancient alluvium might also be occurring within the Monroe syncline and (or) along the Monroe fault or other reverse faults in the current map area. (See discussion of ‘pop-up’ structures in Dragovich and others, 2011.)

Table 3. Major sedimentary provenances for primary Quaternary geologic units in the Monroe, Carnation, North Bend, Fall City, and Snoqualmie 7.5-minute quadrangles. RMFZ, Rattlesnake Mountain fault zone; SWIF, southern Whidbey Island fault zone.

Group	Geologic unit(s)	Provenance	Notes
SP (Snoqualmie or Skykomish Provenance)	Qa (Snoqualmie and Skykomish Rivers), Qc_o, Qc_{ws}, Qc_h, Qc_{pf}	Snoqualmie provenance with generally southeastern fluvial sources; rivers flowing generally northwest along RMFZ–SWIF over time (Dragovich and others, 2010a,b). Ancient and modern Skykomish River alluvium is petrographically similar to ancient and modern Snoqualmie alluvium.	Nonglacial units that contain abundant monocrystalline quartz and significant potassium feldspar, plagioclase and minor but distinct granitic lithic grains, biotite and (or) hornblende; major bedrock source is the Snoqualmie Batholith that covers much of the headwaters of the Snoqualmie River. Rivers trapped in RMFZ–SWIF during nonglacial or interglacial intervals (Dragovich and others, 2010a,b). Structural control of deposition of ancient and modern Skykomish River alluvium might be operative. See Monroe fault and Monroe syncline in Dragovich and others (2011).
LP (Local Provenance)	Qa (Woods Creek), Qc_{ol}	Local provenance with generally eastern sources; rivers flow to the west from the Cascade foothills. Deposited in alluvial, alluvial fan, and swamp settings and likely represent small ancient tributary basin deposits of limited extent. Also see unit Qc_{ol} in Dragovich and others (2010a,b).	Nonglacial units that contain significant local lithic grains including meta-argillite, volcanic lithic grains, metasandstone. Major source of nonglacial units clasts are the volcanic rocks of Mount Persis and the Western mélange belt. Sands are typically lithic rich in the eastern part of the Carnation quadrangle (Dragovich and others, 2010a,b). Sands on Cougar Ridge in the northern part of the Monroe quadrangle have a similar local composition resulting from the reworking of older glacial and nonglacial deposits (Dragovich and others, 2011).
PG (Puget Group Provenance)	Qc_{wp}	Puget Group provenance with fluvial sources to the south and southwest from the Seattle uplift (for example, Tiger Mountain); rivers flowing north to northeast away from the Seattle uplift and toward the ancient Snoqualmie River.	Whidbey Formation (nonglacial) strata in the southwestern portion of the Carnation quadrangle (Dragovich and others, 2010a,b) are sourced by the Puget Group and contain significant andesite detritus as well as some arkosic (feldspathic) sandstone, siltstone from the Tukwila, Renton, and Tiger Mountain Formations. Sands are lithic rich. (See appendices 2–4 in Dragovich and others [2010a] for more information.)
GP (Glacial Provenance)	Qgl_r, Qgos, Qgod, Qgof, Qgic, Qgog, Qgt_v, Qga_v, Qgl_v, Qgt_p, Qgo_p, Qgl_p, Qgd_d	Glacial northern provenance locally mixed with some eastern and northeastern Cascade provenance (particularly for some Vashon recessional deposits sourced by ice-marginal meltwater).	Glacial units contain variable lithic clast types including high-grade metamorphic clasts and contain a high polycrystalline/monocrystalline quartz ratio relative to local Cascade sources and lesser potassium feldspar. Sand grain types tend to be polymictic or variable.

U-PB LA-ICP-MS SINGLE ZIRCON GEOCHRONOLOGY

Introduction and Sample Description

We obtained a uranium-lead (U-Pb) zircon age from a pumiceous lapilli tuff (sample 10-40Y) from unit Evt_{pc} as part of our Monroe quadrangle geologic mapping. Relative probabilty plots versus age plots and age are supplied in Appendix 5 (see Table 1 above for appendix file names).

Methods

Zircons for this study were analyzed for U and Pb isotopes using laser ablation inductively coupled mass spectrometry (LA-ICP-MS) at the University of Alberta Radiogenic Isotope Facility (RIF). A full description of the analytical approach is reported in Simonetti and others (2005). A brief description is provided below.

ZIRCON SEPARATION

About 10 to 15 kg of sample was crushed to fine sand-sized particles. Heavy minerals were then concentrated using a Wilfley table. The zircon concentrate was then passed through a 350 mm sieve and the <350 mm fraction was cleaned by magnetic separation using a Frantz LB1. Zircons were then separated by

density from the nonmagnetic fraction using methylene iodide heavy liquid. From the zircon separate, more than 50 individual zircon grains were selected from the sample and mounted in epoxy. The grain mount was polished to expose the grain centers. Regions suitable for analysis were identified from optical imaging.

LA-ICP-MS

The analytical setup at the RIF consists of a New Wave UP-213 laser ablation system interfaced with a Nu plasma multi-collector inductively coupled plasma mass spectrometer (MC-ICPMS) equipped with three ion counters. We operated the laser at 4 Hz repetition rate at a fluence of ~3 J/cm^2. Laser beam size was 30 mm and pit depth was 25 mm for a typical analysis. Data were collected statically, consisting of 30 1s integrations. Prior to and during each analytical session, zircon reference material GJ1 was analyzed repeatedly and was used to normalize the unknowns, thus correcting for U-Pb fractionation and instrument drift. Mass bias for Pb isotopes was corrected by simultaneously aspirating a 1 ppb Tl solution during ablation.

DATA REDUCTION AND UNCERTAINTIES

All data were reduced offline using an Excel-based program. The uncertainties reported here are quadratic combinations of (1) the standard error ($\sigma/\sqrt{n}$) of the measured isotope ratio, and (2) the standard deviation (σ) of the isotope ratio determinations of the GJ1 standard during the course of the analytical session. Overall uncertainty in age is conservatively estimated to be between 3 and 5% (2 sigma). No common Pb correction was performed on any of the analyses reported here due to the young age of the sample and the uncertainties associated with subtracting the ^{204}Hg background.

Further Information and Interpretation

We obtained a tentative age of 43.7 ±1.0 Ma (n=13, MSWD = 3.7) from the weighted ^{206}Pb/^{238}U average of the youngest zircon grains separated from sample 10-40Y (Appendix 5). The concordia intercept age (anchored to a common Pb value of 0.86 ± 0.06) and TuffZirc age agree within error and are 44.34 ± 0.82 Ma (n=10, MSWD = 1.7) and 44.67 +0.73, -2.15 Ma (n=10, 97.9% confidence) respectively. The age is derived from the statistics of the youngest zircons in the population and likely reflects the eruption age of this tuffaceous pyroclastic deposit. We conservatively estimate the total age uncertainty at ~5% due to possible errors introduced via standard normalization and background subtraction on grains with low count rates for ^{206}Pb. The Eocene age is consistent with other geochronologic data for the volcanic rocks of Mount Persis presented by Tabor and others (1993) and Dragovich and others (2009a). Tabor and others (1993) assigned a late Eocene age to the volcanic rocks of Mount Persis on the basis of a poor apatite fission-track age (47.4 Ma), a hornblende K-Ar age (38.1 Ma), and the observation that the Mount Persis unit is intruded by the Index batholith (34 Ma) and mafic dikes (33 Ma) east of the map area. Dragovich and others (2009a,b) obtained a U-Pb zircon age of 36 ±2.3 Ma (late Eocene) from a thick felsic tuff bed in the Snoqualmie quadrangle southeast of the map area. The Mount Persis volcanism may span several million years (~36–47 Ma) and thus may involve several volcanic centers or volcanoes.

Sample 10-40Y also contains numerous Paleogene-, Mesozoic-, and Proterozoic-age zircons (Appendix 5). The Mount Persis tuff sample 08-55D of Dragovich and others (2009a,b) contains zircons of these general ages, along with a single Cambrian zircon. The older zircons measured were likely incorporated into the parent magma during intrusion—the uniformity of older zircons between the two tuff samples suggests that they assimilated similar rock types—or the zircons were derived by the pyroclastic tuff bodies during extrusion and catastrophic dispersal. Magmatic assimilation may be supported over a pyroclastic origin for these zircons due to a lack of basement rock types in the pyroclastic deposits. A few of the candidates for assimilated underlying geologic units include rocks of the Cretaceous to Jurassic Western mélange belt, or perhaps the Eocene Puget Group (Dragovich and others, 2009a,b,c, 2010a,b; Tabor and others, 1993). Xenocrystic zircons incorporated during magmatic ascent for sample 10-40Y is supported geochemically. Detrital zircon ages from Western mélange belt sandstone (08-45J; Dragovich and others, 2009b) partly overlap the age of xenocrystic zircons within the analyzed Mount Persis tuff samples (samples 10-40Y and 08-55D, above) supporting partial assimilation of mélange belt source rock during parent magma ascent. We note here that the abundant white pumice in tuff sample likely represents primary juvenile volcanic material; this suspicion could be confirmed by directly dating only the pumice clasts in the deposit. The much denser intermediate composition clasts are also primary but may include

variable volcanic detritus excavated from the edifice or incorporated during pyroclastic dispersal. The spread of single-zircon U-Pb ages for sample 10-40Y is consistent with the variety of volcanic lithic grain types in the sample. For example, some of the early Eocene single zircon ages could be derived from incorporation of early Eocene Mount Persis volcanic fragments during the ~44 Ma eruption of tuffaceous pyroclastic flows.

GEOCHEMISTRY OF QUATERNARY SAND DEPOSITS AND THE VOLCANIC ROCKS OF MOUNT PERSIS

Introduction and Methods

New whole rock major and trace elements for two glacial sands, 24 nonglacial sands, and 24 samples from the volcanic rocks of Mount Persis of Tabor and others (1993) were determined by X-ray fluorescence (XRF) and inductively coupled plasma-source mass spectrometer (ICP-MS) at the Geoanalytical Laboratory at Washington State University (WSU)(Appendices 2 and 3).

Grinding of samples was done at WSU using a tungsten carbide mill for XRF analyses and iron equipment for ICP-MS analyses. Estimates of accuracy and precision as well as discussion of analytical methods for both XRF and ICP-MS at WSU are given in Johnson and others (1999) and Knaack and others (1994) respectively. Before grinding, all 26 Quaternary sediments were sieved with 2 and 0.075 mm sieves at the DNR laboratory in Olympia, Washington, so that only the sand-sized fraction was chemically analyzed. This was done to eliminate erroneous results that may occur from large gravel-size clasts and to remove the variable amounts of silt and clay from these sandy samples. Using this technique, we provide a better comparison between the glacially and nonglacially derived sediments by assuring that we are only comparing the composition of the sands rather than comparing sands with silty sands.

Geochemical data for Holocene alluvium and older nonglacial sands from the Fall City and the adjacent Carnation 7.5-minute quadrangles (Dragovich, 2007; Dragovich and others, 2010b,c) are included in the sand geochemical discussion. We also include geochemical data from a lahar, a breccia, two flows and two vitric tuffs of the Eocene volcanic rocks of Mount Persis from the nearby Snoqualmie and Carnation 7.5-minute quadrangles (Dragovich and others, 2009a,b; 2010a). The geochemical data, sample petrography, and other sample information are supplied as an electronic attachment (Appendix 2). Additionally, the locations of the geochemical samples for the Monroe quadrangle are provided in Appendix 3. All samples are plotted on a loss on ignition-free basis.

Quaternary Sand Geochemistry

Major- and trace-element geochemistry of sediments can provide invaluable information about their original tectonic setting and provenance (Roser and Korsch, 1986; McLennan and others, 1993). Biogenic $CaCO_3$ or SiO_2, high concentrations of heavy minerals or quartz, as well as diagenetic reactions related to burial can affect the concentrations of elements within a sedimentary sample (Galloway, 1974; Roser and Korsch, 1986, 1988; McLennan, 1989). Thus, caution should be used when making interpretations based only on geochemical analyses of sediments, and ratios should be used whenever possible. These samples are not normalized CaO-free to correct for carbonate, as suggested by Roser and Korsch (1986, 1988), because petrography indicates that they lack carbonate minerals (Appendix 2).

HOLOCENE NONGLACIAL DEPOSITS

Alluvium (unit Qa)—Six alluvial SP sands, including one sample from the Fall City 7.5-minute quadrangle (Dragovich, 2007) and four samples from the Carnation 7.5-minute quadrangle (Dragovich and others, 2010a), plot within the intermediate igneous provenance field on the Roser and Korsch (1988) provenance discriminant function diagram (Fig. 1A). They have chondrite-normalized La/Lu ratios between 3.83 and 5.98, and Ba + Sr between 658 and 730 parts per million (ppm) (Fig. 1B). These sands have SiO_2, in weight percentage (wt%), between 70.63 and 72.63; $CaO+Na_2O$ between 5.74 and 6.23 wt%; Al_2O_3 between 13.55 and 14.53 wt%; K_2O between 1.26 and 1.59 wt%; TiO_2 between 0.53 and 0.68 wt%; and $FeO^T + MgO$ between 5.84 and 6.65 wt% (Appendix 4, Fig. 1). Alluvium sands plot within the active continental margin field on the Roser and Korsch (1986) log K_2O/Na_2O vs. SiO_2 tectonic discrimination diagram (Appendix 4, Fig. 2). They plot within the continental arc field, with one sample (06-60D from Dragovich, 2007) plotting in the overlap with active continental margins on the Al_2O_3/SiO_2 vs. $Fe_2O_3{}^T+MgO$ sandstone tectonic discriminant diagram of Bhatia, 1983 (Appendix 4, Fig. 3). The alluvium sands have a chemical index of

alteration (CIA)(Nesbitt and Young, 1989; Nesbitt, 2003) that ranges from 53.60 to 55.87 (Appendix 4, Fig. 4).

PLEISTOCENE GLACIAL AND NONGLACIAL DEPOSITS

Fluvial outwash deposits (unit Qgof)—One outwash sand from this unit (10-10L) plots within the intermediate igneous provenance field on Figure 1A. This sand has a chondrite-normalized La/Lu ratio of 4.57, and Ba+Sr of 707 ppm (Fig. 1B). This outwash sand has a SiO_2 of 76.69 wt%; $CaO+Na_2O$ of 5.40 wt%; Al_2O_3 of 11.64 wt%; K_2O of 1.12 wt%; TiO_2 of 0.37 wt%; and FeO^T+MgO of 4.63 wt% (Appendix 4, Fig. 1). The Qgof sand plots within the active continental margin field on Figure 2 of Appendix 4. It also plots within the active continental margins field on Figure 3 of Appendix 4. The CIA of this outwash sand is 52.58 (Appendix 4, Fig. 4).

Vashon advance outwash (unit Qga_v)—Two sands from this unit, 09-7F from Dragovich and others (2010a, b) and 10-13N from this study, plot within the intermediate igneous provenance field on Figure 1A. They have chondrite-normalized La/Lu ratios between 3.93 and 5.04, and Ba+Sr between 597 and 643 ppm (Fig. 1B). Unit Qga_v sands have SiO_2 between 73.65 and 74.44 wt%; $CaO+Na_2O$ between 5.15 and 5.78 wt%; Al_2O_3 between 12.20 and 13.76 wt%; K_2O between 1.01 and 1.65 wt%; TiO_2 between 0.50 and 0.68 wt%; and FeO^T+MgO between 5.16 and 5.68 wt% (Appendix 4, Fig. 1). These two advance outwash sands plot within the active continental margin field on Figure 2 of Appendix 4. On Figure 3 of Appendix 4, sample 10-13N plots near the field for active continental margins; while sample 09-7F (Dragovich and others, 2010a,b) plots within the continental arc-active continental margins overlap field and has a CIA that ranges from 52.38 to 56.26 (Appendix 4, Fig. 4).

Olympia beds of Minard and Booth (1988), Snoqualmie and Skykomish River provenance (unit Qc_o)—Eighteen sands were chemically analyzed from this unit: one from the Fall City quadrangle (Dragovich, 2007), thirteen from the Carnation quadrangle (Dragovich and others, 2010a,b), and four from this study. Sixteen of the Qc_o sands plot within the intermediate igneous provenance field on Figure 1A. Sample 10-1J plots within the mafic igneous provenance field, and sample 10-24D plots near the intermediate igneous-mafic igneous provenance boundary (Fig. 1A). They have chondrite-normalized La/Lu ratios between 3.54 and 5.85, and Ba+Sr between 556 and 821 ppm (Fig. 1B). The Qc_o sands have SiO_2 between 69.97 and 75.96 wt%; $CaO+Na_2O$ between 3.52 and 7.05 wt%; Al_2O_3 between 11.08 and 14.54 wt%; K_2O between 0.98 and 1.65 wt%; TiO_2 between 0.34 and 0.68 wt%; and, FeO^T+MgO between 3.74 and 9.54 wt% (Appendix 4, Fig. 1). All eighteen sands plot within the active continental margin field on Figure 2 of Appendix 4. On Figure 3 of Appendix 4, seven samples plot within or near the active continental margins field, three samples plot within or near the continental arc field, and seven samples plot within or near the active continental margins-continental arc overlap. Sample 10-1J plots at a higher $Fe_2O_3^T+MgO$ value than other Qc_o sample and near the field for oceanic arc (Appendix 4, Fig. 3). Seventeen of the Qc_o sands have a CIA that ranges from 50.58 to 56.65; while sample 10-24D has a higher CIA of 64.44 (Appendix 4, Fig. 4).

Whidbey Formation, Snoqualmie and Skykomish River provenance (unit Qc_{ws})—Ten sands from Qc_{ws} have been chemically analyzed; five from the Carnation quadrangle (Dragovich and others, 2010a,b) and five from this study. Nine of the Qc_{ws} sands plot within the intermediate igneous provenance field on Figure 1A; while sample 09-7A plots within the mafic igneous provenance field (Fig. 1A). They have chondrite-normalized La/Lu ratios between 3.86 and 5.69, and Ba+Sr between 606 and 837 ppm (Fig. 1B). The Qc_{ws} sands have SiO_2 between 72.81 and 76.18 wt%; $CaO+Na_2O$ between 4.89 and 6.15 wt%; Al_2O_3 between 11.17 and 13.84 wt%; K_2O between 0.96 and 1.66 wt%; TiO_2 between 0.41 and 0.61 wt%; and FeO^T+MgO between 5.05 and 6.72 wt% (Appendix 4, Fig. 1). All ten samples plot within the active continental margin field on Figure 2 of Appendix 4. On Figure 3 of Appendix 4, six samples plot within or near the active continental margins-continental arc overlap field, and four samples plot near the active continental margins field. These ten Qc_{ws} sands have a CIA that ranges from 50.60 to 57.39 (Appendix 4, Fig. 4).

Hamm Creek formation, Snoqualmie and Skykomish River provenance (unit Qc_h)—Four sands from Qc_h have been chemically analyzed. All of these samples chemically analyzed have a Skykomish provenance (Appendix 2). Three of the Qc_h sands plot within the intermediate igneous provenance field on Figure 1A, while sample 10-8D plots within the mafic igneous provenance field (Fig. 1A). Unit Qc_h sands have chondrite-normalized La/Lu ratios between 4.39 and 5.41, and Ba+Sr between 645 and 849 ppm (Fig. 1B).

The Qc_h sands have SiO_2 between 69.08 and 73.95 wt%; $CaO+Na_2O$ between 4.41 and 6.79 wt%; Al_2O_3 between 13.43 and 14.61 wt%; K_2O between 1.11 and 1.30 wt%; TiO_2 between 0.46 and 0.80 wt%; and FeO^T+MgO between 4.94 and 8.90 wt% (Appendix 4, Fig. 1). All four Qc_h sands plot within the active continental margin field Figure 2 of Appendix 4. On Figure 3 of Appendix 4, sand 10-46A plots within or near the active continental margins field, sand 10-24C plots within and sand 10-24B plots near the continental arc field, and sand 10-8D plots near the oceanic arc field. These four Qc_h sands have a CIA that ranges from 51.85 to 54.01; also, sample 10-8D has a higher CIA of 69.75 (Appendix 4, Fig. 4).

Pre-Fraser continental nonglacial deposits, Snoqualmie and Skykomish River provenance (unit Qc_{pf})—Thirteen sands from Qc_{pf} have been chemically analyzed. Five of the samples are from the Carnation quadrangle (Dragovich and others, 2010a,b) and eight of the samples are from this study. Eight of the Qc_{pf} sands plot within the intermediate igneous provenance field on Figure 1A. Five sands, two from the Carnation quadrangle and three from this study, plot within the mafic igneous provenance field (Fig. 1A). These sands have chondrite-normalized La/Lu ratios between 3.98 and 5.59, and Ba+Sr between 563 and 839 ppm (Fig. 1B). The Qc_{pf} sands have SiO_2 between 61.58 and 77.86 wt%; $CaO+Na_2O$ between 3.94 and 6.63 wt%; Al_2O_3 between 10.72 and 20.88 wt%; K_2O between 0.97 and 1.35 wt%; TiO_2 between 0.29 and 0.88 wt%; and FeO^T+MgO between 3.41 and 9.43 wt% (Appendix 4, Fig. 1). Twelve of the Qc_{pf} sands plot within the active continental margin field on Figure 2 of Appendix 4. Sample 09-37D plots in the arc field (Appendix 4, Fig. 2). On Figure 3 of Appendix 4, three sands plot within and three sands plot near the active continental margins field, two sands plot within and three sands plot near the continental arc field, sand 10-37A plots near the active continental margin-continental arc field, and sand 09-37D plots near the oceanic arc field. Twelve of the Qc_{pf} sands have a CIA that ranges from 50.93 to 57.64, while sample 09-37D has a higher CIA of 64.56 (Appendix 4, Fig. 4).

Quaternary Sand Geochemistry—General Findings

NONGLACIAL SAND PROVENANCE

The majority of the nonglacial SP (Table 3) sands did not undergo high amounts of chemical alteration (Appendix 4, Fig. 4); the chemistry of these samples reflects the composition of their original provenances (Nesbitt and Young, 1989; McLennan and others, 1993; Nesbitt, 2003). In general, SP nonglacial sands from the Fall City, Carnation, and Monroe 7.5-minute quadrangles plot within the intermediate igneous provenance field on Figure 1A, have moderate to high large ion lithophile element concentrations (for example, La, Ba, Sr, Rb, Pb, and Th; Appendix 2; Fig. 1B), and many plot within or near the continental arc field on the sandstone tectonic discriminant diagram of Bhatia (1983)(Appendix 4, Fig. 3). Qc_{pf} sand plots within the arc field on Figure 2 of Appendix 4. SP nonglacial sands also plot within the active continental margin field on the Roser and Korsch (1986) log K_2O/Na_2O vs. SiO_2 tectonic discrimination diagram (Appendix 4, Fig. 2), and a number of samples plot within or near the active continental margin field on Figure 3 of Appendix 4. This suggests that these sands are predominantly derived from an intermediate arc source with minor recycled terrigenous components (Roser and Korsch, 1986, 1988; Floyd and others, 1991; McLennan and others, 1990, 1993; McDonough and Sun, 1995; McLennan, 2001). SiO_2 contents for these sands are higher than intermediate compositions (Appendix 2; Appendix 4, Fig. 1), however, this may be attributed to the concentration of silicates after sieving the samples to remove the silts and clay fraction. Sand petrography (Appendix 2) and provenance (Table 3) corroborate these interpretations.

Figure 1A displays that eight SP nonglacial samples, five from unit Qc_{pf} and one sample each from units Qc_o, Qc_{ws}, and Qc_h, plot within the mafic igneous provenance field on the Roser and Korsch (1988) provenance discriminant function diagram. Two of these sands (10-1J and 10-56D) have chondrite-normalized La/Lu ratios and Ba+Sr values that are lower than other SP sands (Fig. 1B). Three of these SP sands (09-37D, 09-43G-1, and 10-44W) have $CaO+Na_2O$ wt% that is ≥ 5.86; two sands (09-37D and 10-8D) have TiO_2 wt% that is ≥ 0.80; and three of these sands (09-37D, 10-1J, and 10-8D) have FeO^T+MgO wt% ≥ 8.90 (Appendix 4, Fig. 1). Also, Qc_{pf} sand 09-37D from Dragovich and others (2010a,b), Qc_o sand 10-1J, and Qc_h sand 10-8D plot near the oceanic arc field on Figure 3 of Appendix 4. The geochemical data is consistent with a less evolved, more mafic source for some of the SP nonglacial sands that mixed with a more evolved arc source (Bhatia, 1983; Roser and Korsch, 1988; Floyd and others, 1991; McLennan and others, 1990, 1993; McDonough and Sun, 1995; McLennan, 2001). The sand petrography (Appendix 2) and provenance (Table 3) corroborate these interpretations.

As stated above, petrography of the nonglacial modern and ancient sands indicate that they have a Skykomish or Snoqualmie provenance (Appendix 2; Table 3). The tectonic and provenance discrimination diagrams (Fig. 1A; Appendix 4, Fig. 2 and 3), trace elements (Fig. 1B; Appendix 2), and major elements (Appendix 2; Appendix 4, Fig. 1 and 4) do not distinguish Skykomish from Snoqualmie provenance samples. The only minor difference is that Snoqualmie provenance sands may have slightly higher SiO_2 and slightly lower Al_2O_3 average values than Skykomish provenance sands (Appendix 4, Fig. 1). Unit Qa sands also cannot be chemically distinguished from ancient nonglacial sands (Fig. 1A and B; Appendix 4, Fig. 1, 2, 3, and 4). This supports the petrographic observation that both modern and ancient SP sands are derived from a similar basin sources.

GLACIAL SAND PROVENANCE

An additional ten glacially derived sands from older studies (Dragovich, 2007; Dragovich and others, 2010a,b) are plotted on all figures with the two samples from this study. The glacial sands did not undergo high amounts of chemical alteration (Appendix 4, Fig. 4); the chemistry of these samples reflects the composition of their original provenances (Nesbitt and Young, 1989; McLennan and others, 1993; Nesbitt, 2003). Glacially derived sands generally have moderate large ion lithophile element concentrations (for example, La, Ba, Sr, Rb, Pb, and Th; Appendix 2; Fig. 1B). They all plot within the active continental margin field on Figure 2 of Appendix 4. Also, ten sands plot in or near the active continental margins field on Figure 3 of Appendix 4, while two sands plot within the active continental margins-continental arc overlap (Appendix 4, Fig. 3). Eleven of the glacial sands plot within the intermediate igneous provenance field on Figure 1A, while one sample plots in the mafic igneous provenance field. This suggests that the glacial sands have a provenance that is rich in accreted sedimentary and metamorphic terranes (for example, Western mélange belt) as well as an intermediate arc source (Roser and Korsch, 1986, 1988; Floyd and others, 1991; McLennan and others, 1990, 1993; McDonough and Sun, 1995; McLennan, 2001).

Geochemical Discrimination of Glacial versus Nonglacial Sand Deposits

Mahoney and others (2003), Saltonstall and others (2003), and Mahoney (2007) all had success geochemically distinguishing glacial from nonglacial Quaternary sediments in this region. We are also able to discriminate between glacial and nonglacial sands using geochemistry. The glacially derived sands generally have lower average chondrite-normalized La/Lu ratios, Ba + Sr, $CaO+Na_2O$, Al_2O_3, TiO_2, FeO^T+MgO, Rb, Pb, and Zr values than nonglacial sands (Fig. 1B; Appendix 2; Appendix 4, Fig. 1) (Dragovich, 2007; Dragovich and others, 2010a). The lower chondrite-normalized La/Lu ratios suggest that the glacially derived sands originated from a provenance that was not as enriched as the nonglacially derived sands (McDonough and Sun, 1995). Ba, Sr, Rb, and Pb have higher concentrations in felsic rocks and upper continental crust (McLennan, 2001), thus the nonglacially derived sands may have a slightly more felsic source than nonglacial sands. Zr is concentrated in the heavy mineral zircon, which originates in felsic to intermediate igneous rocks, and can become concentrated by the transportation and recycling of sediments (McLennan, 1989; McLennan and others, 1993). Also, the higher $CaO+Na_2O$ and Al_2O_3 contents in the nonglacially derived sands suggest that they are richer in feldspar than the glacially derived sands, while the higher TiO_2 and FeO^T+MgO contents suggest that the nonglacially derived sands have more ferromagnesian minerals, such as biotite and hornblende, than the glacially derived sands (Appendix 4, Fig. 1). These findings are supported by the sand petrography (Appendix 2) and provenance (Table 3). The geochemical differences outlined above suggest that the glacial sands have a larger accreted sedimentary and metamorphic terrane provenance than nonglacial sands; further, nonglacial sands originated from a slightly more felsic igneous source and (or) were transported farther than the glacially derived sands.

Five glacial samples have chondrite-normalized La/Lu ratios that are similar to nonglacial SP sands (Fig. 1B). Four of these samples also have Ba+Sr values that are similar to nonglacial SP sands (Fig. 1B). The field setting and petrography of these samples (Dragovich and others, 2010a, 2011; Appendix 2) suggest that this is a result of glacial sands being partially derived from the erosion of older underlying nonglacial sands. For example, sample 09-7B from unit Qgik is a kame deposit partially derived from nonglacial Whidbey Formation (Qc_{WS}) that stratigraphically sits directly below the kame (Dragovich and others, 2010b). Six of the nonglacial SP sands have chondrite-normalized La/Lu ratios and Ba+Sr values similar to glacial samples (Fig. 1B). The field setting and petrography of these samples (Dragovich and others, 2010a,b, 2011) suggest that this is a result of the alluvium undercutting slopes that contain glacial sands. Also, alluvial fans or mass wasting could have also mixed the glacial and nonglacial sands. These

samples have sedimentary and metamorphic lithics as well as chert clasts that support the incorporation of glacial sands and can account for the transitional geochemistry (Appendix 2; Fig. 1B; Table 3).

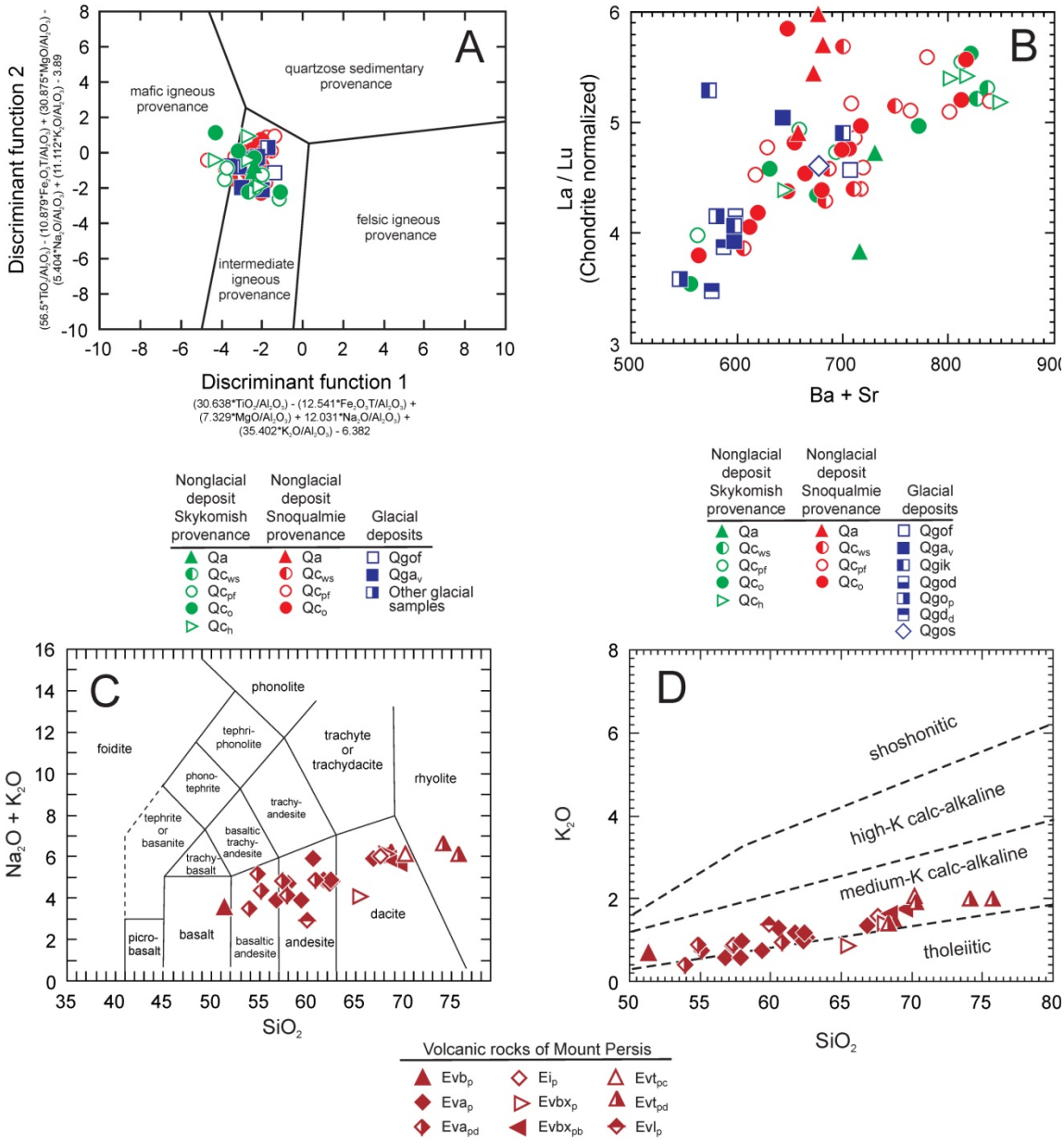

Figure 1. A. Sands from the Monroe 7.5-minute quadrangle plotted on the discriminant function diagram for the provenance of sedimentary rocks (after Roser and Korsch, 1988). **B.** Chondrite normalized La/Lu vs. Ba + Sr (ppm) diagram for nonglacial and glacial sands from Monroe, Carnation, and Fall City 7.5-minute quadrangles (Dragovich, 2007). Normalization values from McDonough and Sun (1995). **C.** Volcanic rocks of Mount Persis (Tabor and others, 1993) plotted on the total-alkalis vs. silica diagram of Le Maitre and others (2002).
D. K_2O vs. SiO_2 diagram for the volcanic rocks of Mount Persis (Tabor and others, 1993) displaying the subdivision of subalkalic rocks. Fields compiled by Rollinson (1993). Volcanic rocks of Mount Persis includes data from Snoqualmie, Carnation, and Monroe 7.5-minute quadrangles (Dragovich and others, 2009).

Igneous Rock Geochemistry of the Volcanic Rocks of Mount Persis

A significant data set of 30 samples now exists for the volcanic rocks of Mount Persis. This includes 24 new samples reported here for the first time, three samples from the Snoqualmie 7.5-minute study of

Dragovich and others (2009a,b), and three samples from the Carnation 7.5-minute study of Dragovich and others (2010a,b). General geochemical observations of the volcanic rocks of Mount Persis are reported below.

Flows and intrusions (units Evb_p, Eva_p, Eva_{pd}, and Ei_p)—On the total alkali-silica (TAS) diagram, sample10-45H, map unit Evb_p, plots within the basalt field (Fig. 1C). Nine flows from unit Eva_p plot within the andesite field (Fig. 1C); two of these samples, 08-76H and 09-15M, are from Dragovich and others (2009a,b; 2010a,b), respectively. Flow 10-25F from Eva_p plots within the dacite field on the TAS diagram (Fig. 1C). The dark aphanitic flows (Eva_{pd}) plot within the basaltic andesite and andesite fields on the TAS diagram (Fig. 1C). Sample 10-36W, from map unit Ei_p, plots within the dacite field on Figure 1C. On the K_2O vs. SiO_2 diagram, most samples from these map units plot within the medium-K calc-alkaline field (Fig. 1D). Three Eva_p samples (10-15G and 10-19D from this study and 08-76H from Dragovich and others, 2009a,b) and two Eva_{pd} samples (10-8J and 10-33F) plot near the tholeiitic-calc-alkaline boundary (Fig. 1D). The aluminum saturation indices (ASI)(Frost and others, 2001) of the flows are predominantly less than 1 (Appendix 2; Appendix 4, Fig. 5); also, they have molecular Na+K that is less than molecular Al (Appendix 2, which indicates that they are metaluminous). One Eva_p (08-76H) and one Ei_p (10-36W) sample have an ASI that is greater than 1 (Appendix 2; Appendix 4, Fig. 5) and are peraluminous. On the Th/Yb-Ta/Yb tectonic discrimination diagram (Pearce, 1982, 1983), units Eva_p, Eva_p, and Ei_p plot within the calc-alkaline and continental arcs fields (Appendix 4, Fig. 6). One Eva_p and one Eva_{pd} sample (10-4J and 10-15G respectively) plot close to the mantle array on this diagram (Appendix 4, Fig. 6). The Evb_p sample plots within the mantle array, near enriched mantle sources, on Figure 6 of Appendix 4. On the Ce/Nb-Th/Nb diagram (Saunders and others, 1988) the Evb_p samples plots near enriched mantle sources with a Ce/Nb value of 1.73 and a Th/Nb value of 6.83 (Appendix 4, Fig. 7). Samples for map units Eva_p, Eva_{pd} and Ei_p have Ce/Nb values that range from 2.45 to 4.38 and Th/Nb values that range from 0.12 to 0.42 (Appendix 4, Fig. 7).

Volcanic breccia, bomb breccia, tuff, and lahar (units $Evbx_p$, $Evbx_{pb}$, Evt_{pc}, Evt_{pd}, Evl_p) —A pyroclastic breccia (09-13N) from Dragovich and others (2010a,b), two bomb breccia clasts, two lithic tuffs, one from Dragovich and others (2010a, b) and one from this study, a lapilli tuff (10-40Y), and three Evt_{pd} vitric tuffs plot within the dacite field on the TAS diagram (Fig. 1C); while two vitric tuffs from Dragovich and others (2009a,b) (08-5H and 08-44J) plot within the rhyolite field on the TAS diagram (Fig. 1C). One clast from a semicohesive thick lahar bed plots within the andesite field on the TAS diagram (Fig. 1C). On the K_2O vs. SiO_2 diagram, most samples from these map units, except 09-13N from Dragovich and others (2010a,b), plot within the medium-K calc-alkaline field (Fig. 1D). Sample 09-13N, map unit $Evbx_p$, is a lithic tuff from Dragovich and others (2010a,b) that plots near the tholeiitic-calc-alkaline boundary (Fig. 1D). All of these samples have an ASI greater than 1 (Appendix 2; Appendix 4, Fig. 5), indicating that they are peraluminous; however, some lahar clasts (sample 09-31Q from Dragovich and others, 2010a,b) also have a high CIA (~67), suggesting that Al could have been concentrated during alteration of this sample. On the Th/Yb-Ta/Yb tectonic discrimination diagram (Pearce, 1982, 1983), units $Evbx_p$, $Evbx_{pb}$, Evt_{pc}, Evt_{pd}, and Evl_p plot within the calc-alkaline and continental arcs fields (Appendix 4, Fig. 6); however, three vitric tuffs and one lapilli tuff plot near the calc-alkaline-shoshonitic boundary on this diagram (Appendix 4, Fig. 6). On the Ce/Nb-Th/Nb diagram (Saunders and others, 1988) these units have Ce/Nb values that range from 3.29 to 6.44 and a Th/Nb values that range from 0.26 to 0.49 (Appendix 4, Fig. 7).

Volcanic Rocks of Mount Persis Interpretations

The volcanic rocks of Mount Persis of Tabor and others (1993) are principally medium-K calc-alkaline with fewer subunits that are transitional to tholeiitic (Fig. 1D; Appendix 4, Fig. 6). Their ASI is metaluminous at lower SiO_2 values, but peraluminous at higher SiO_2 values (Appendix 2; Fig. 1C; Appendix 4, Fig. 5). This indicates that assimilation increased as the Mount Persis magma evolved. The dacitic and rhyolitic samples also have higher Ce/Nb and Th/Nb ratios, with many samples trending towards or plotting near the average value of continental crust (Fig. 1C; Appendix 4, Fig. 7). This supports the observation that assimilation increased as the magmas evolved, and as stated above (U-Pb Geochronology) it suggests that continental crust may have been the material that was assimilated into the magma. Appendix 6 indicates that a tuff from unit Evt_{pc} has numerous xenocrystic zircons, which is in agreement with a high degree of assimilation. The Th/Yb, Th/Nb, and Ce/Nb ratios of these samples

indicate that they evolved from partial melting of an enriched mafic mantle source (Appendix 4, Fig. 6 and 7)(Pearce, 1982, 1983). The basalt sample (10-45H; Evb_p) has trace element concentrations that may reflect the composition of the magma's primary source (Appendix 4, Fig. 6 and 7). This unit's peraluminous to metaluminous, predominantly medium-K calc-alkaline composition, with elevated Th/Yb and Ce/Nb ratios, suggests that the volcanic rocks of Mount Persis formed in a "Corderillan-type" continental arc (Pearce, 1983; Frost and others, 2001).

ISOSTATIC GRAVITY AND AEROMAGNETIC DATA FOR THE MONROE QUADRANGLE

Methods

GEOPHYSICAL MAP

Aeromagnetic data used here come from a survey contracted by the U.S. Geological Survey in 1997. Flight lines are oriented north–south and have a 250-m spacing (Blakely and others, 1999). Magnetic anomalies for the map area are strongly asymmetric with respect to their source, therefore we present a reduced-to-pole aeromagnetic anomaly map (Appendix 6, Fig. A), calculated using standard procedures (Blakely, 1995). This filter moves magnetic anomalies directly over the magnetic source units. For interpretation purposes, we upward continue the reduced-to-pole magnetic grid to 50 m above the flight altitude and then subtract the product from our original magnetic grid. The result is a map that isolates the anomalies produced by near-surface magnetic rocks. (See aeromagnetic map and geophysical model cross sections on map sheet of Dragovich and others [2011].) Recent data constrain the gravity anomalies for this region (Anderson and others, 2006; Dragovich and others, 2007, 2009a,c, 2010a,b). Standard formulas and reduction procedures (Blakely, 1995), as well as a reduction density of 2670 kg/m^3 for the crust, constrain the isostatic gravity anomaly contours.

GEOPHYSICAL MODELING

We use the GM-SYS Geophysical Modeling software (NGA, Inc.) to produce our geophysical cross section models. Sampling of the magnetic grid for the model profile is 250 m, the same as the spacing of flight lines on the aeromagnetic survey. Magnetic measurement altitudes in the profile match the airplane altitude recorded by radar altimeter during the aeromagnetic survey. Gravity constraint is considerably sparser, more on the order of a grid with spacing of 1 km between stations (Dragovich and others, 2011; Appendix 6, Fig. A). We only display gravity data points on the profiles that lie within 1.5 km of the profile line. Therefore, some of the details that are less than 1 km in width on the profile, which are based on geologic mapping, though matching the existing gravity grid are not well constrained. Our modeling procedure honors both the mapped lithologic boundaries and any known thicknesses of Quaternary sediments across the profiles. In addition, dips of beds measured at the surface are consistent with folded materials below, with most of these structurally inferred dips matching the gravity and magnetic anomalies very well. Geophysical evidence as well as structural inference and regional geologic map relationships (for example, Tabor and others, 1993) generally constrains deeper boundaries. Model A (Dragovich and others, 2011) is a smaller part of a larger model (Appendix 6, Fig. B), which we needed to provide a background trend in the computed gravity and magnetic anomalies; smaller amplitude and wavelength anomalies overprint these larger trends and result from smaller scale structure within the structural cross section. (See aeromagnetic map and geophysical model cross sections on map sheet of Dragovich and others, [2011].)

ROCK PHYSICAL PROPERTIES

Hand samples and outcrop magnetic susceptibility measurements, as well as hand sample density measurements (Anderson and others, 2006; Appendix 6, Fig. C) support density and magnetic properties of the rock units used in the map interpretation and two-dimensional geophysical modeling. Where density and magnetic susceptibility measurements are not available, we apply reasonable densities from past geophysical modeling in the region (Dragovich and others, 2007; 2009a,c; 2010a,b). Geophysical properties of 'combined' units are averages from hand samples of each component, based on the percentage of each component exposed in or estimated from outcrops in the area. For example, the volcanic rocks of Mount Persis of Tabor and others (1993)(Mt. Persis) contains more magnetic units (basalt flows) in the western part of the quadrangle than the east, therefore we model it with a greater density and magnetic

susceptibility in the west. Basement properties are computed in the same way (Appendix 6, Fig. C), but we modify them in our geophysical models based on modeling from areas farther to the west in the Puget Lowland (Anderson and others, 2006, 2008). Physical properties of units used during the modeling process may be slightly different from hand sample values (within reasonable limits based on standard deviations of all samples for the unit and expected lithostatic compression with depth) to allow better data fit of the models to geophysical anomalies in this region.

Interpretation

GEOPHYSICAL MAP

The most magnetic geologic unit of the quadrangle is the basalt flows (unit Evb_p) of the volcanic rocks of Mount Persis. A single outcrop of basalt (geochemically confirmed) in the region supports this inference, which spatially correlates with a strong magnetic anomaly (BA in Appendix 6, Fig. A). A gravity high is also tenuously associated with this outcrop, though only supported by one gravity measurement. In addition, strong aeromagnetic anomalies in the southwestern part of the quadrangle over the Seattle basin (basin edges inferred from the isostatic gravity gradients) require a very strongly magnetic unit in the subsurface (BF in Appendix 6, Fig. A). It is possible that a component of these strong magnetic anomalies result from basaltic andesites (unit Eva_{pd}) within the Mt. Persis, however none of our hand sample measurements of this portion of the Mt. Persis have high enough susceptibility to account for the strength of the anomaly (Appendix 6, Fig. C). Previously, we interpreted a correlation between this laterally extensive magnetic high and magnetic rocks within the Blakeley Formation (Dragovich and others, 2010a,b). We revise this interpretation in this report because of the association of magnetic highs with basalt outcrops (Dragovich and others, 2011) and lack of magnetic material in exposed Blakeley Formation beds we examined within the west-adjacent Maltby 7.5-minute quadrangle. Based on the spatial limitation of the basaltic flows within the SE highlands on the quadrangle (BC in Appendix 6, Fig. A), it is likely that regions containing basalts were either river channels (BC in Appendix 6, Fig. A) or a lowland basin (BF in Appendix 6, Fig. A). It is the inverse relationship between extensive high magnetic anomaly (BF) and the low gravity anomaly associated with the Seattle basin that leads to the interpretation of highly magnetic basaltic flows filling the basin (Appendix 6, Fig. B). This is consistent with the general interpretation of high-magnetization basalt-flow-dominated packages within the unit originating as more fluid, farther-traveling volcanic flows (potential source to the east/northeast). Conversely, low-magnetization clastic, tuffaceous, and volcaniclastic packages dominate the volcanic rocks of Mt. Persis in the SE highlands. Andesite flows in the region are also magnetic and contribute to smaller magnetic anomalies associated with the SE highlands. This concept is a new interpretation of magnetic anomalies in the region (contrasting with Dragovich and others, 2007, 2009a,b, 2010a,b), which have been interpreted largely with respect to varying percentages of magnetic andesites (Appendix 6, Fig. C) incorporated within the volcanic rocks of Mount Persis. We model the magnetic densities and susceptibilities of the Western mélange to be uniform with respect to depth; however, it is locally variable in nearby regions (Dragovich and others, 2009a,b,c; Appendix 6, Fig. C).

Isostatic gravity anomalies largely reflect the Seattle basin deepening westward, thus the observed overall gradient with decreasing anomaly values to the southwest (Appendix 6, Fig. A; Dragovich and others, 2011). In addition, we interpret a shallower and smaller basin correlated with a gravity low along the Skykomish River (SL in Appendix 6, Fig. A). Faults are also interpreted to generally follow local gravity gradients as well as a few magnetic gradients, with strongest support for reverse offset on the Cherry Valley, Monroe, and High Rock faults (Appendix 6, Fig. A). Locations of faults coincide with mathematically determined maximum gradients computed for both the isostatic gravity and reduced-to-pole (RTP) aeromagnetic anomaly data. The reverse sense of offset along several faults, supported by the high gravity anomaly over the SE highlands (HH in Appendix 6, Fig. A) establishes the SE topographic highlands also as a structural highland.

GEOPHYSICAL CROSS SECTION MODELS

Due to the complexity of the subsurface geology, there are many possible subsurface rock geometries that will fit our geophysical data. Because of this, we modified cross sections A and B (Dragovich and others, 2011) from original structural inference to fit the observed gravity and magnetic data in order to keep our

models as geologically and structurally reasonable as possible. Increase in sediment density with depth broadly follows Anderson and others (2006). The position of fault-bounded rock packages matches well with the initial determinations derived solely from structural-stratigraphic inferences in the geologic cross section models. The only exception is the High Rock fault, which we projected from the east into cross section B–B′ on the basis of the gravity and magnetic data, and interpreted as a reverse fault accommodating large total offsets. Aeromagnetic highs to the south of both models A and B influence the magnetic anomalies on both lines. We incorporated off-line bodies to account for these anomalies, which are not shown on the models in Dragovich and others (2011) or in Appendix 6, Fig. B. These bodies have magnetic susceptibility and density as well as depth appropriate to the volcanic rocks of Mount Persis, including basaltic flows, and are similar to values shown for Mt. Persis in model A. The thickness of the Mt. Persis units west of Rattlesnake Mountain fault (RMF) no. 1 in Appendix 6, Fig. B, likely also includes units of the Puget Group, especially to the western end of the model, but we did not separate these two units within the modeling process because they would be very hard to distinguish at that depth.

Distinctions between different types of 'Seattle basin fill' (Miocene units, Blakeley Formation, Puget Group, volcanic rocks of Mount Persis) are not distinguishable by the gravity data. Adjustments in the depth of boundaries between different units trade off with their densities. What is generally reflected in the gravity anomaly data is the general increase in sediment depth to the west and the large jump in sediment thickness at the Cherry Valley fault, which is supported by an increase in gravity gradient across this significant structure. It is interesting to note that the large gravity gradient is along the Cherry Valley fault in this quadrangle, but to the south in the Carnation quadrangle it is along Rattlesnake Mountain fault no. 1 (RMF1)(Dragovich and others, 2010a). As in the Carnation quadrangle, the Snoqualmie Valley fault no. 1 (SVF1) produces the best fit to the gravity and magnetic anomalies, having only minor reverse offset; in the Monroe quadrangle, the western fault block is displaced up relative to the eastern block—the opposite of the displacement along this fault in the Carnation quadrangle. Though this fits best with the gravity and magnetic anomalies across this part of the model, the dominant anomalies arise from the syncline/anticline pair within the block bounded by SVF1 and the Cherry Valley fault (Dragovich and others, 2011; Appendix 6, Fig. B). Major down-to-the-west vertical offset is needed in the larger model A (Appendix 6, Fig. B) across a fault that is likely RMF1, based on its position along strike with this fault on the Carnation quadrangle and along the same gradient in the isostatic gravity map.

Although cataclasites (unit tz) along faults typically have low densities, it is not as critical for modeling the gravity data here as it is further south (for example, North Bend quadrangle of Dragovich and others, 2009c) because of the possible trade off with density of overlying sedimentary units. They are included based on: (1) observations of cataclasite or deformed Pleistocene deposits (unit Qtz) along the Cherry Valley fault within the map area; (2) observation of broad zones of unit tz along some of these faults both in the Monroe quadrangle and in quadrangles south of the map area (Dragovich and others, 2007, 2009a,b,c, 2010a,b, 2011); and (3) our contention that some of the faults (such the Cherry Valley fault) are major and long-lived structures that have a accumulated much permanent strain.

The basalt flows (unit Evb_p) within the volcanic rocks of Mount Persis between SVF1 and the Cherry Valley fault on model A are schematic and their distribution within the Mt. Persis is diagrammatic rather than fixed. We based the percentage of basalt versus other rocks on what best fit the observed gravity and magnetics. Individual basalt flows shown within the SE highlands are modeled as individual units, but their placement and susceptibility is also not fixed. The basalt flow within the basin associated with the Skykomish River on model B is supported by basalt outcropping to the west of the line as well as a magnetic high associated with that outcrop, which bleeds east onto the line itself. The two faults with the largest reverse offset on model B (Monroe and High Rock faults) are supported both by gravity gradients and offset on an inferred basalt unit crossing both faults. Few alternate geometries are possible based on extensive testing of the model space permitted by the gravity and magnetic anomalies across these faults and surface mapping constraints. A variation in thickness of basalt is the only nonfixed parameter that is geologically feasible and consistent with surface mapping. As discussed extensively for the Carnation quadrangle (Dragovich and others, 2010a), Sherrod and others (2008) also use a magnetic Mt. Persis unit in modeling of geophysical data in this region, and the aeromagnetic high BF in this quadrangle is contiguous with their anomaly B. However, we use a much higher susceptibility for the Mt. Persis unit in our models (c = 50-57 x 10^{-3} SI maximum in our region as opposed to c = ~24 x 10^{-3} SI for Sherrod and others, 2008) and include the magnetic units as flows within a shallower but thinner Mt. Persis unit, contrasting with the model of Sherrod and others (2008). The overall thickness we propose for the Mt. Persis unit is more consistent with regional geologic mapping of the unit, as well as with the observation that the volcanic

center(s) for the volcanic rocks of Mount Persis are to the east of the geophysical model lines. Though we handle the modeling of this unit differently than Sherrod and others (2008), our overall tectonic conclusions are the same: our data and modeling support reverse offset on steeply dipping faults in the region. Because the Mt. Persis unit thickens across faults along line A (Dragovich and others, 2011; Appendix 6, Fig. B), an implication of our model is that these faults were probably active at the time of its eruption; conversely, Mt. Persis units do not change at fault boundaries in model B, therefore, their offset likely postdates Mt. Persis eruption.

EARTHQUAKE EPICENTERS IN AND NEAR THE MONROE QUADRANGLE

We obtained the hypocenters shown on Plates 1 and 2 from Pacific Northwest Seismic Network. The earthquake catalog data were initially downloaded from the Advanced National Seismic System (ANSS) website (http://quake.geo.berkeley.edu/anss/catalog-search.html). We analyzed the hypocenters using ZMAP, a tool for visualizing seismicity patterns (Wyss and others, 2001). The hypocenters southeast of the Monroe 7.5-minute quadrangle and its vicinity were included in our analyses because the May 2, 1996, Duvall (M5.2) earthquake occurred in this area and provides main shock and volumes of aftershock information in the area. To better interpret the complex tectonic structure where the Duvall earthquake occurred, we relocated the events recorded after Duvall earthquake. The hypoDD algorithm is based on ray paths from two earthquakes close to a common station being almost identical, and the difference in observed travel time can therefore be attributed with a high degree of certainty to the spatial offset of the two earthquakes (Hartog and others, 2008; Dragovich and others, 2009c). The hypoDD algorithm (Waldhauser and Ellsworth, 2000) uses earthquake pick files. (Pick files obtained from the Pacific Northwest Seismic Network [PNSN]; S. Malone, PNSN, 2011, pers. commun.) We did not use cross correlation of waveforms but suspect only minor displacement of hypocenters from a cross-correlation analysis. To understand general behavior of the fault mechanism for the area, we also downloaded 44 focal mechanism solutions (http://www.pnsn.org) for the Duvall earthquake area. Because relocated earthquakes' hypocenter locations changed only mildly (< 2 km for focal depths and < 1 km for epicenter locations), we kept and analyzed identification numbers with the corresponding focal mechanism solutions. These relocated hypocenter changes did not affect the focal mechanism solutions much, < 5 degrees in strike, dip and rake. Therefore, we directly used the PNSN focal mechanism solutions without recalculating them from relocated earthquake pick files (updated phase data, found from the hypoDD relocation calculations). Then P and T axes determined from the focal mechanism information (called AM cards) were used to prepare a ternary plot (Lees, 1999, 2007, 2008) of the Duvall area events. To select earthquakes, we included only those events for which we have pick file data (to be able to verify quality of picks) and that had a duration magnitude (Md) of 1.0 or more. This resulted in 608 events, of which we were able to successfully relocate 521 for the Duvall area (Plate 2, Fig. 2). We also relocated a total of 1792 PNSN catalog earthquakes (1969–2011) of variable size and quality that occurred in and around the Monroe 7.5-minute quadrangle (Plate 1).

Interpretation

Plate 1 provides the hypocenters and focal mechanism data for the Monroe 7.5 minute quadrangle and surrounding area. Outside the Duvall area (including the 7.5 minute Monroe quadrangle area) shallower and deeper crustal earthquakes are well distributed in a depth range of 0 to 30 km. The faults to the west of the Monroe quadrangle are from Sherrod and others (2005, 2008). Noteworthy observations include: (1) the higher incidence of small earthquakes along the apparent projection of the Cherry Valley fault or nearby faults near Devils Butte in the west-adjacent Maltby 7.5-minute quadrangle (hypocenters are relatively deep, suggesting that these earthquakes might not be related to faults or lineaments mapped at the surface); and (2) the occurrence of a small cluster of shallow earthquakes along the projection of the Cherry Creek fault zone (CCFZ) northeast of the Monroe quadrangle in the northeastern part of Plate 1. Note the Duvall earthquake swarm in the southeastern corner of the Monroe quadrangle on Plate 1.

The May 2, 1996, Duvall earthquake epicenters (max. M_L=5.3 or Md=5.4) originated at a shallow depth (~2–8 km) along the CCFZ (Dragovich and others, 2010a,b, 2011). Plate 2 shows the Duvall earthquake swarm hypocenters and focal mechanisms in detail. The majority of the microearthquakes, including aftershocks of Duvall earthquake, occurred in a depth range of 2 to 8 km (relocated events). We interpret the focal mechanism data to indicate that these earthquakes occurred along several faults within a left-lateral strike-slip fault zone flower structure. In this scenario, fault displacements and strain are partitioned between both (1) left-lateral, high-angle, northeast-trending faults, *and* (2) lower angle,

northeast-trending reverse faults or thrusts in the CCFZ. We suspect the thrusts and reverse faults are anastomosing structures that link the high-angle faults. This scenario is supported by the focal mechanism data presented in Figure 2 and Plate 2, which shows that most displacements have either have a *left-lateral northeast-trending solution or* a northeast-trending thrust solution. (Left-lateral offset is indicated for the focal mechanisms with northeast-trending high-angle faults on Plate 2). It is also supported by the field mapping and outcrop structures that show that the CCFZ is dominated by northeast-trending fault splays with strike-slip kinematics. In conclusion, the CCFZ is: (1) associated with a long lineament suggesting a high-angle fault (Plate 1); and (2) the dominance of thrust and strike-slip focal mechanisms suggesting partitioning of displacements between high-angle strike-slip faults and shallowly dipping faults within a flower structure as illustrated on Figure 2c.

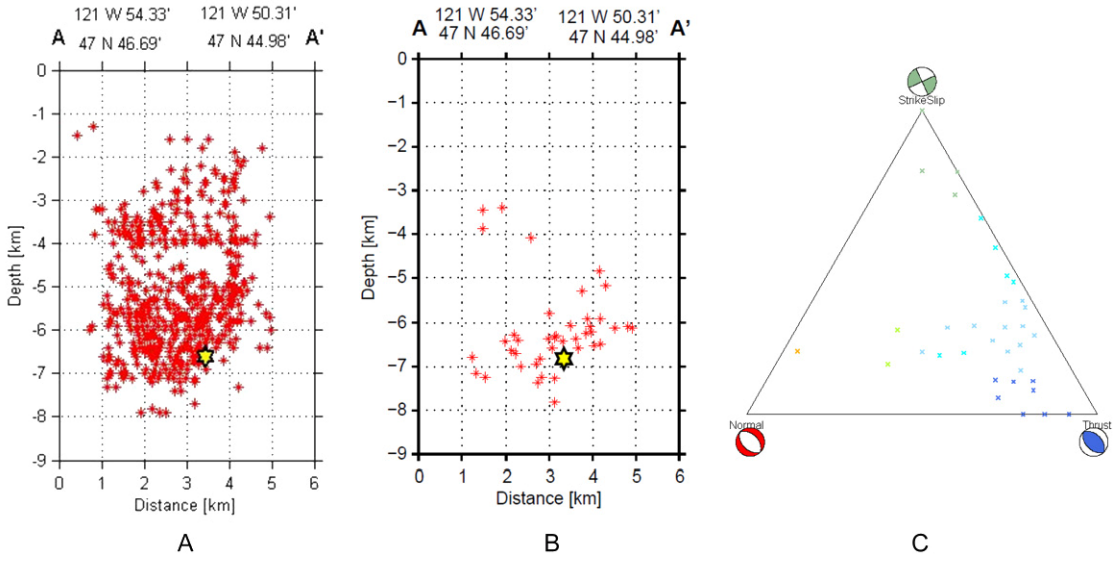

Figure 2. Duvall earthquake swarm information. Cross sections (Figs. 2a and 2b) of the Duvall earthquake swarm are located on Plate 2. **Figure 2a.** All the micro and moderate earthquakes in the swarm. **Figure 2b.** Only Duvall earthquakes with focal mechanisms. See Plate 2 for epicenter locations of the focal mechanisms within the CCFZ. Cross sections are plotted using the ZMAP tool (Wyss and others, 2001). **Figure 2c.** Ternary diagram showing the variation in focal mechanisms for the Duvall earthquake. The dominance of thrust and strike-slip focal mechanism on this ternary diagram suggests partitioning of displacements between strike-slip faults and shallower faults within a positive flower structure.

QUATERNARY DEFORMATION

Introduction

Obtaining direct field evidence for Holocene motion on fault strands in the region is complicated by the dense vegetative cover and urbanization. In lieu of trenching on suspected fault traces, fault investigations must rely on sparse outcroppings near topographic, geomorphic, and geophysical lineaments. Faults were mapped in the Monroe 7.5-minute quadrangle by Dragovich and others (2011) on the basis of our interpretation of geophysical anomalies, geomorphologic lineaments, and stratigraphy, as well as our interpretation of deformational features observed in outcrop both locally and regionally (Dragovich and others, 2007, 2009a,b,c, 2010a,b). Photographs of a few of the Quaternary deformational or liquefaction features observed in the map area are presented in Appendix 7.

Neotectonic Features—Tectonic Deformation and Liquefaction

Liquefaction features are widespread and locally very intense in the pre-Vashon nonglacial deposits of the map area (units Qc_o, Qc_{ws}, Qc_{pf}, and Qc_h in Appendix 7) and rarely some of the glacial deposits (unit Qgl_v). Liquefaction features include sand dikes, flames, destroyed or chaotic bedding, rootless tight to isoclinal folding, and rare dish structures. In many areas, moderately intense to intense liquefaction was observed in successive nonglacial exposures, giving the impression that large volumes of strata had been liquefied. Although liquefaction is not restricted to the nonglacial deposits and has been noted in some Vashon glacial deposits, the intense and widespread occurrence of liquefaction in SP units (Table 3) implies

that the ancient Snoqualmie or Skykomish River depositional environments were favorable for past liquefaction events. It is widely known that because alluvium is predominately saturated and loose, these granular deposits have a high potential for liquefaction. Given this potential, it begs the question: does the bulk of the liquefaction observed in ancient SP deposits record liquefaction concurrent with past deposition as flat-lying ancient Snoqualmie or Skykomish River deposits? It could be argued that the widespread nature of this *low to moderate intensity liquefaction* in the SP units seems best explained as spatially broad liquefaction resulting from earthquakes, perhaps regional earthquakes. However, the general volume of liquefied sediment relative to undisturbed sediment observed in areas away from probable active faults suggests (but does not prove) that much of the causative shaking must be local and related to nearby active faults such as the RMFZ–SWIF. (In other words, although not quantified, our regional perspective is that the Pleistocene nonglacial units in the Snoqualmie valley contain a high of volume of nonglacial sediments with liquefaction features compared to similar Pleistocene nonglacial deposits in most other areas in the Puget Sound basin.) We suspect the confluence of other indicators of neotectonism, such as fault scarps and lineaments (Sherrod and others, 2008), anomalously high and thick ancient alluvial SP bodies, and tilted and folded Quaternary strata, indicate that the widespread liquefaction in ancient SP units we observed is the result of local tectonism along the RMFZ–SWIF. It is important to note that some small faults or fractures in liquefied beds might be ancient mass-wasting features related to lateral spreading. During earthquakes, liquefied bodies spread toward an open face such as a river terrace via lateral spreading, and some lateral-spread landslide scarps could have an appearance similar to tectonic fractures or faults.

Individual Fault Features in the Monroe Quadrangle—Summaries and Activity

ACTIVITY

Quaternary tectonic deformational features observed in the map area include fractures and broad folding located around apparently active folds. Some of the mapped faults are considered probable active faults, but definitive evidence of Holocene activity awaits further study (for example, detailed fault trenching). *Active faults* as described here are considered to have evidence for offset during the Holocene (last ~11,000 yrs). The best evidence for active faulting includes displaced Holocene deposits combined with other evidence for on-going displacement such as hypocenters along faults. *Potentially active faults* as described here have evidence for offset during Quaternary time, which has been recently expanded to include the last ~2.6 million years. There is good evidence that several of the mapped faults in the study area are *potentially active* faults with seismic evidence for *active* displacement along the Cherry Creek fault zone. Complete characterization of these mapped faults awaits detailed analyses, including fault trenching for both the proposed active faults and potentially active faults.

FAULT SUMMARIES

Here we document some of the attributes for the three faults mapped by Dragovich and others (2011). The Rattlesnake Mountain fault zone (RMFZ) is a regional strike-slip fault zone that likely correlates with the southern Whidbey Island fault (SWIF) of Dragovich and others (2009a,b,c; 2010a,b; 2011) and Sherrod and others (2008). All of the discussed faults (except the Monroe fault and associated structures) were originally mapped south of the Monroe quadrangle (Dragovich and others, 2007, 2009a,b,c, 2010b) and extended into this area. (See "Overview of Quaternary Tectonic Features" in the Snoqualmie valley in Dragovich and others [2010a] for further information.)

Cherry Valley fault (CVF)—The northwest-trending CVF, which may correlate with the Griffin Creek fault of Dragovich and others (2009a,b; 2010a,b), is interpreted to be the northeastern boundary of the Seattle basin in the Monroe quadrangle. Evidence that the CVF is active or potentially active is tentatively made on the basis of (1) probable tectonic deformation of Quaternary deposits (unit Qc_{pf}) near the fault, and (2) possible spatial association of the extension of this fault with earthquake hypocenters. (See "Earthquake Hypocenters in and near the Monroe Quadrangle".) We also observed distinctly fractured and liquefied ancient Snoqualmie River alluvium (unit Qc_{pf}) at site 28D in the Maltby quadrangle near the extension of the Cherry Valley fault. (See radiocarbon information in Appendix 1 and site 28D photos on p. 50 and 51.) We suspect these deposits are deformed by Quaternary offset along the Cherry Creek fault that projects to near this site and appears to align with fault scarps and lineaments mapped by Sherrod and others (2005,

2008) along the southwestern slopes of Devils Butte in the Maltby 7.5-minute quadrangle to the west. Additionally, Dragovich and others (2009a,b; 2010a,b) tentatively related some geophysical and (or) topographic lineaments in the Snoqualmie and Carnation quadrangles to active tectonism along the Griffin Creek fault and CVF.

Cherry Creek fault zone—Dragovich and others (2010a,b) termed a family of subparallel faults in the northeastern part of the Carnation quadrangle the Cherry Creek fault zone (CCFZ). The northeast-trending CCFZ may be a conjugate fault zone to the overall right-lateral and northwest-trending RMFZ. This arrangement is strikingly similar to the relationship between the Tokul Creek fault zone and the RMFZ in the Snoqualmie quadrangle southeast of the present map area and east of the City of Snoqualmie—the Tokul Creek fault appears to be regional fault zone that juxtaposes basement, with or without thin overlying Tertiary volcanic rocks, against thicker Tertiary volcanic rocks (Dragovich and others, 2009a,b). In both cases, the northeast-trending faults may be conjugate faults to the RMFZ–SWIF system where the northeast-trending Tokul Creek fault zone merges with the northwest-trending RMFZ. Part of the Tokul Creek fault was originally mapped by Tabor and others (1993). Although no distinct lidar lineaments or Quaternary deformation along the Tokul Creek fault were noted by Dragovich and others (2009a), the occurrence of several earthquake hypocenters near the Tokul Creek fault zone suggests a locally active structure. Earthquake focal mechanism data suggest that the Tokul Creek fault zone is currently accommodating left-lateral strike-slip displacement (Dragovich and others, 2009a) similar to the CCFZ. The northeast-trending CCFZ also appears to be a left-lateral conjugate fault zone to the active right-lateral SWIF structure. Outcrop structures including fractures and slickenlines, as well as the physical orientation of the fault lineaments, indicate a zone dominated by high-angle strike-slip faults. We interpret the focal mechanisms associated with the shallow Duvall earthquake swarm to indicate a positive flower structure associated with a transpressional left-lateral strike-slip fault zone. (See "Earthquake Hypocenters in and near the Monroe Quadrangle'.) Dragovich and others (2010a,b) tentatively relate local Quaternary deformation of unit Qc_{ol} to tectonism within the CCFZ south of the Monroe quadrangle. Conversely, we found no direct field evidence for an active fault zone along the CCFZ strands in the Monroe quadrangle. However, the spatial correspondence of the shallow earthquakes (2–10 km depth) with a high-angle fault zone is strongly suggestive of an active fault, and the lack of tectonic scarps might be due to masking by vegetative cover and mass wasting along the steep slopes common within the fault zone.

Monroe fault and reverse faults on the SE highlands—The Monroe fault is a geophysical lineament that is subparallel to several probable fold axes near the Skykomish River in the Monroe quadrangle. We tentatively hypothesize that this fault and other reverse faults mapped in the SE highlands might be potentially active structures responsible for the folding and uplift of Pleistocene nonglacial deposits (ancient alluvium) perched on the highlands. This uplift might be part of a broad pop-up structure related to transpression on the SWIF as discussed in Dragovich and others (2011).

APPENDICES

See Table 1 at the beginning of this document for the filename of electronically attached appendices.

ACKNOWLEDGMENTS

This geologic map was funded in part by the U.S. Geological Survey (USGS) National Cooperative Geologic Mapping Program under award no. G10AC00363. We thank many people for assistance: field assistant Julia Labadie and Monroe mapping team members Curtis Koger, Jennifer Saltonstall, Bruce Stoker, and John Bethel; Dan Smith (King County DNRP/WLRD) for helping with some field mapping; Benjamin Perry for office help with GIS and other data; Steve Malone (PNSN) for help with downloading the pick files used for the relocation algorithm; Renate Hartog (PNSN) are providing information on the UW pick files for the relocation algorithm; Jonathan Lees (Univ. of North Carolina) for providing R scripts; Robert Morin (USGS emeritus) for providing gravity data within and northwest of the Monroe quadrangle. We also thank the following Washington Division of Geology and Earth Resources colleagues: Tim Walsh for help with the lidar data, Lee Walking for assistance with references, and Jari Roloff , Jessica Czajkowski, and Karen Meyers for editing this report.

REFERENCES CITED

Aitken, M. J., 1985, Thermoluminescence dating: Academic Press [London], 359 p.

Anderson, M. L.; Blakely, R. J.; Brocher, T. M.; Pratt, T. L.; Wells, R. E.; Haugerud, R.; Bush, M., 2006, Structure of the Seattle uplift from seismic, gravity, magnetic, geologic, and geomorphic data: Eos (American Geophysics Union Transactions), v. 87, no. 52, Supplement, Abstract T41A-1554.

Anderson, M. L.; Dragovich, J. D.; Blakely, R. J.; Wells, Ray; Brocher, T. M., 2008, Where does the Seattle fault end?—Structural links and kinematic implication [abstract]: Eos (American Geophysical Union Transactions), v. 89, no. 53, Suppl., p. F2535-F2536.

Associated Earth Sciences, Inc., 1999, Environmental impact statement—Soils, geology, geologic hazards, and water quality, Cougar Ridge and Old Owen Place, Snohomish County, Washington. *In* Associated Earth Sciences, Inc., 2010, Monroe quadrangle reports: Associated Earth Sciences, Inc., [excerpts].

Bhatia, M. R., 1983, Plate tectonics and geochemical composition of sandstones: Journal of Geology, v. 91, no. 6, p. 611-627.

Blakely, R. J., 1995, Potential theory in gravity and magnetic applications: Cambridge University Press, 441 p.

Blakely, R. J.; Wells, R. E.; Weaver, C. S., 1999, Puget Sound aeromagnetic maps and data: U.S. Geological Survey Open-File Report 99-514, version 1.0. [http://pubs.usgs.gov/of/1999/of99-514/]

Booth, D. B., 1990, Surficial geologic map of the Skykomish and Snoqualmie Rivers area, Snohomish and King Counties, Washington: U.S. Geological Survey Miscellaneous Investigations Series Map I-1745, 2 sheets, scale 1:50,000, with 22 p. text.

Dragovich, J. D., 2007, Sand point count and geochemical data in the Fall City and Carnation 7.5-minute quadrangles, King County, Washington: Washington Division of Geology and Earth Resources Open File Report 2007-3, 2 Microsoft Excel files with 6 p. text. [http://www.dnr.wa.gov/Publications/ger_ofr2007-3_fallcity_supplement.zip]

Dragovich, J. D.; Anderson, M. L.; MacDonald, J. H., Jr.; Mahan, S. A; DuFrane, S. A.; Littke, H. A.; Wessel, G. R.; Saltonstall, J. H.; Koger, C. J.; Cakir, Recep, 2010a Supplement to the geologic map of the Carnation 7.5-minute quadrangle, King County, Washington—Geochronologic, geochemical, point count, geophysical, earthquake, fault, and neotectonic data: Washington Division of Geology and Earth Resources Open File Report 2010-2, 42 p., 8 digital appendices. [http://www.dnr.wa.gov/Publications/ger_ofr2010-2_carnation_supplement.zip]

Dragovich, J. D.; Anderson, M. L.; Mahan, S. A.; Koger, C. J.; Saltonstall, J. H.; MacDonald, J. H., Jr.; Wessel, G. R.; Stoker, B. A.; Bethel, J. P.; Labadie, J. E.; Cakir, Recep; Bowman, J. D.; DuFrane, S. A., 2011, Geologic map of the Monroe 7.5-minute quadrangle, King and Snohomish Counties, Washington: Washington Division of Geology and Earth Resources Open File Report 2011-1, 1 sheet, scale 1:24,000, with 24 p. text. [http://www.dnr.wa.gov/publications/ger_ofr2011-1_geol_map_monroe_24k.zip]

Dragovich, J. D.; Anderson, M. L.; Walsh, T. J.; Johnson, B. L.; Adams, T. L., 2007, Geologic map of the Fall City 7.5-minute quadrangle, King County, Washington: Washington Division of Geology and Earth Resources Geologic Map GM-67, 1 sheet, scale 1:24,000. [http://www.dnr.wa.gov/Publications/ger_gm67_geol_map_fallcity_24k.zip]

Dragovich, J. D.; Littke, H. A.; Anderson, M. L.; Hartog, Renate; Wessel, G. R.; DuFrane, S. A.; Walsh, T. J.; MacDonald, J. H., Jr.; Mangano, J. F.; Cakir, Recep, 2009a, Geologic map of the Snoqualmie 7.5-minute quadrangle, King County, Washington: Washington Division of Geology and Earth Resources Geologic Map GM-75, 2 sheets, scale 1:24,000. [http://www.dnr.wa.gov/Publications/ger_gm75_snoqualmie_24k.zip]

Dragovich, J. D.; Littke, H. A.; Anderson, M. L.; Wessel, G. R.; Koger, C. J.; Saltonstall, J. H.; MacDonald, J. H., Jr.; Mahan, S. A.; DuFrane, S. A., 2010b, Geologic map of the Carnation 7.5-minute quadrangle, King County, Washington: Washington Division of Geology and Earth Resources Open File Report 2010-1, 1 sheet, scale 1:24,000, 21 p. text. [http://www.dnr.wa.gov/Publications/ger_ofr2010-1_geol_map_carnation_24k.zip]

Dragovich, J. D.; Littke, H. A.; MacDonald, J. H., Jr.; DuFrane, S. A.; Anderson, M. L.; Wessel, G. R.; Hartog, Renate, 2009b, Geochemistry, geochronology, and sand point count data for the Snoqualmie 7.5-minute quadrangle, King County, Washington: Washington Division of Geology and Earth Resources Open File Report 2009-4, 35 p. text, 3 Microsoft Excel files. [http://www.dnr.wa.gov/Publications/ger_ofr2009-4_snoqualmie_suppl.zip]

Dragovich, J. D.; Walsh, T. J., 2008, Geochemical sample analyses of Tertiary and pre-Tertiary volcanic rocks in and around the North Bend 7.5-minute quadrangle, King County, Washington: Washington Division of Geology and Earth Resources Open File Report 2008-4, 6 p. text with 1 Excel file on DVD. [http://www.dnr.wa.gov/Publications/ ger_ofr2008-4_northbend_geochem.zip]

Dragovich, J. D.; Walsh, T. J.; Anderson, M. L.; Hartog, Renate; DuFrane, S. A.; Vervoot, Jeff; Williams, S. A.; Cakir, Recep; Stanton, K. D.; Wolff, F. E.; Norman, D. K.; Czajkowski, J. L., 2009c, Geologic map of the North Bend 7.5-minute quadrangle, King County, Washington, with a discussion of major faults, folds, and basins in the map area: Washington Division of Geology and Earth Resources Geologic Map GM-73, 1 sheet, scale 1:24,000. [http://www.dnr.wa.gov/Publications/ger_gm73_geol_map_northbend_24k.zip]

Duller, G.A.T., 2008, Luminescence dating—Guidelines on using luminescence dating in archeology: English Heritage [Swindon, UK], 43 p.

Floyd, P. A.; Shail, R.; Leveridge, B. E.; Franke, W., 1991, Geochemistry and provenance of Rhenohercynian synorogenic sandstones—Implications for tectonic environment discrimination. *In* Morton, A. C.; Todd, S. P.; Haughton, P. D. W., Developments in sedimentary provenance studies: Geological Society [London] Special Publication 57, p. 173-188.

Forman, S. L.; Pierson, J., 2002, Late Pleistocene luminescence chronology of loess deposition in the Missouri and Mississippi River valleys, United States: Palaeogeography, Palaeoclimatology, Palaeoecology, v. 186, no. 1 and 2, p. 25-46.

Frost, B. R.; Barnes, C. G.; Collins, W. J.; Arculus, R. J.; Ellis, D. J.; Frost, C. D., 2001, A geochemical classification for granitic rocks: Journal of Petrology, v. 42, no. 11, p. 2033-2048.

Galloway, W. E., 1974, Deposition and diagenetic alteration of sandstone in northeast Pacific arc-related basins—Implications for greywacke genesis: Geological Society of America Bulletin, v. 85, issue 3, p. 379-390.

Hartog, Renate; Gomberg, J.; Moran, S.; Wright, A.; Meagher, K., 2008, The October 8, 2006 M4.5 Cowlitz Chimney earthquake in Mount Rainier National Park: Seismological Research Letters, v. 79, no. 2, p. 186-193.

Johnson, D. M.; Hooper, P. R.; Conrey, R. M., 1999, XRF analysis of rocks and minerals for major and trace elements on a single low dilution Li-tetraborate fused bead: Advances in X-ray Analysis, v. 41, p. 843-867. [http://www.sees.wsu.edu/Geolab/note/V41_91.pdf]

Knaack, C.; Cornelius, S.; Hooper, P., 1994, Trace element analysis of rocks and minerals by ICP/MS: Department of Geology Washington State University Open-file Report, December 1994, 18 p.

Le Maitre, R. W.; Streckeisen, A.; Zanettin, B.; Le Bas, M. J.; Bonin, B.; Bateman, P., eds., 2002, Igneous rocks—A classification and glossary of terms; 2nd ed.: Cambridge University Press [Cambridge, U.K.], 256 p.

Lees, J. M., 1999, Geotouch—Software for three and four-dimensional GIS in the earth sciences**:** Computers & Geosciences, v. 26, no. 7, p. 751-761.

Lees, J. M., 2007, RFOC—Graphics for spherical distributions and earthquake focal mechanisms, graphics for statistics on a sphere, as applied to geological fault data, crystallography, earthquake focal mechanisms, radiation patterns, ternary plots and geographical/geological maps: Comprehensive R Archive Network (CRAN). [accessed May 31, 2011, at http://streaming.stat.iastate.edu/CRAN/web/packages/RFOC/index.html].

Lees, J. M., 2008, GEOmap—Topographic and geologic mapping: Comprehensive R Archive Network (CRAN) [accessed May 31, 2011, at http://streaming.stat.iastate.edu/CRAN/web/packages/GEOmap/index.html].

Mahan, S. A.; Miller, D. M.; Menges, C. M.; Yount, J. C., 2007, Late Quaternary stratigraphy and luminescence geochronology of the northeastern Mojave Desert: Quaternary International, v. 166, p. 61-78.

Mahoney, B. J.; Prindiville, S.; Troost, K. G.; Booth, D. B., 2003, Geochemical characteristics of glaciogenic sediments, Puget Lowland, Washington: Geological Society of America Abstracts with Programs, v. 35, no. 6, p.79.

Mahoney, J. B., 2007, Quaternary sediments geochemical analytical data—Redmond Ridge East UPD/FCC and Panhandle preliminary plat [prepared for Associated Earth Sciences, Inc.]: J. Brian Mahoney unpublished report, 51 p.

McDonough, W. F.; Sun, S. S., 1995, The composition of the Earth: Chemical Geology, v. 120, p. 223-253.

McLennan, S. M., 1989, Rare earth elements in sedimentary rocks—Influence of provenance and sedimentary processes: Reviews in Mineralogy and Geochemistry, v. 21, no. 1, p. 169-200.

McLennan, S. M., 2001, Relationships between the trace element composition of sedimentary rocks and upper continental crust: Geochemistry, Geophysics, Geosystems, v. 2, no, 4, p. 1021-1045, doi:10.1029/2000GC000109.

McLennan, S. M.; Hemming, S.; McDaniel; D. K.; Hanson, G. N., 1993, Geochemical approaches to sedimentation, provenance, and tectonics. *In* Johnson, M. J.; Basu, A., eds., Processes controlling the composition of clastic sediments: Geological Society of America Special Paper 284, p. 21-40.

McLennan, S. M.; Taylor, S. R.; McCulloch, M. T.; Maynard, J. B., 1990, Geochemical and Nd-Sr isotopic composition of deep-sea turbidites; Crustal evolution and plate tectonic associations: Geochimica et Cosmochimica Acta, v. 54, no. 7, p. 2015-2050.

Minard, J. P.; Booth, D. B., 1988, Geologic map of the Redmond quadrangle, King County, Washington: U.S. Geological Survey Miscellaneous Field Studies Map MF-2016, 1 sheet, scale 1:24,000. [http://ngmdb.usgs.gov/Prodesc/proddesc_5609.htm]

Murray, A. S.; Marten, R.; Johnston, A.; Martin, P., 1987, Analysis for naturally occurring radionuclides at environmental concentrations by gamma spectrometry: Journal of Radioanalytical and Nuclear Chemistry, Article 115, no. 2, p. 263-288.

Murray, A. S.; Wintle, A. G., 2003, The single aliquot regeneration dose protocol—Potential for improvements in reliability: Radiation Measurements, no. 37, p. 377-381.

Nesbitt, H. W., 2003, Petrogenesis of siliciclastic sediments and sedimentary rocks. *In* Lentz, D. R., ed., Geochemistry of sediments and sedimentary rocks—Evolutionary considerations to mineral deposit-forming environments: Geological Association of Canada, GeoTex 4, p. 39-51.

Nesbitt, H. W.; Young, G. M., 1989, Formation and diagenesis of weathering profiles: Journal of Geology, v. 97, no. 2, p. 129-147.

Pearce, J. A., 1982, Trace element characteristics of lavas from destructive plate boundaries. *In* Thorpe, R. S., ed., Andesites—Oogenic andesites and related rocks: John Wiley & Sons [Chichester, U.K.], p. 525-548.

Pearce, J. A., 1983, Role of the subcontinental lithosphere in magma genesis at active continental margins. *In* Hawksworth, C. J.; Norry, M. J., eds., Continental basalts and mantle xenoliths: Shiva Publishing [Nantwich, Great Britain], p. 230-249.

Prescott, J. R.; Hutton, J. T., 1994, Cosmic ray contributions to dose rates for luminescence and ESR dating—Large depths and long-term time variations: Radiation Measurements, v. 23, p. 497-500.

Richardson, C. A.; McDonald, E. V.; Busacca, A. J., 1997, Luminescence dating of loess from the northwest United States: Quaternary Science Reviews, v. 16, no. 3-5, p. 403-415.

Rollinson, H. R., 1993, Using geochemical data; evaluation, presentation, interpretation: Prentice Hall [London, England], 352 p.

Roser, B. P.; Korsch, R. J., 1986, Determination of tectonic setting of sandstone-mudstone suites using SiO_2 content and K_2O/Na_2O ratios: Journal of Geology, v. 94, p. 635-650.

Roser, B. P.; Korsch, R. J., 1988, Provenance signatures of sandstone-mudstone suites determined using discriminant function analysis of major-element data: Chemical Geology, v. 67, p. 119-139.

Saltonstall, J. H.; Koger, C. J; Sweet, Suzanne; Thompson, S. S., 2003, Olympia age paleotopographic influences on Vashon glaciofluvial sedimentation beneath eastern Bear Creek plateau, King County, Washington [abstract]: Geological Society of America Abstracts with Programs, v. 35, no. 6, p. 109.

Saunders, A. D.; Norry, M. J.; Tarney, J., 1988, Origin of MORB and chemically-depleted mantle reservoirs—Trace element constraints: Journal of Petrology, Special Volume 1, p. 379-414.

Sherrod, B. L.; Blakely, R. J.; Weaver, Craig; Kelsey, Harvey; Barnett, Elizabeth; Wells, Ray, 2005, Holocene fault scarps and shallow magnetic anomalies along the southern Whidbey Island fault zone near Woodinville, Washington: U.S. Geological Survey Open-File Report 2005-1136, 35 p. [http://pubs.usgs.gov/of/2005/1136/]

Sherrod, B. L.; Blakely, R. J.; Weaver, C. S.; Kelsey, H. M.; Barnett, Elizabeth; Liberty, Lee; Meagher, K. L.; Pape, Kristin, 2008, Finding concealed active faults—Extending the southern Whidbey Island fault across the Puget Lowland, Washington: Journal of Geophysical Research, v. 113, B05313, doi:10.1029/2007JB005060, 2008.

Simonetti, Antonio; Heaman, L. M.; Hartlaub, R. P.; Creaser, R. A.; MacHattie, T. G.; Bohm, Christian, 2005, U-Pb zircon dating by laser ablation-MC-ICP-MS using a new multiple ion counting Faraday array: Journal of Analytical Atomic Spectrometry, v. 20, no. 8, p. 677-686.

Singhvi, A. K.; Sharma, Y. P.; Agrawal, D. P., 1982, Thermo-luminescence dating of sand dunes in Rajasthan, India: Nature, v. 295, p. 313-315.

Snyder, S. L.; Duval, J. S., 2003, Design and construction of a gamma-ray spectrometer system for determining natural radioactive concentrations in geological samples at the U.S. Geological Survey in Reston, Virginia: U.S. Geological Survey Open-File Report 03-29, [on-line only]. [http://pubs.usgs.gov/of/2003/of03-029/]

Sun, S. S.; McDonough, W. F., 1989, Chemical and isotopic systematics of oceanic basalts; Implications for mantle composition and processes. *In* Saunders, A. D.; Norry, M. J., eds., Magmatism in the ocean basins: Geological Society Special Publications, no. 42, p. 313-345.

Tabor, R. W.; Frizzell, V. A., Jr.; Booth, D. B.; Waitt, R. B.; Whetten, J. T.; Zartman, R. E., 1993, Geologic map of the Skykomish River 30- by 60-minute quadrangle, Washington: U.S. Geological Survey Miscellaneous Investigations Series Map I-1963, 1 sheet, scale 1:100,000, with 42 p. text. [http://pubs.usgs.gov/imap/i1963/]

Troost, K. G.; Booth, D. B.; Wisher, A. P.; Shimel, S. A., 2005, The geologic map of Seattle—A progress report: U.S. Geological Survey Open-File Report 2005-1252, version 1.0, 1 sheet, scale 1:24,000. [http://pubs.usgs.gov/of/2005/1252/]

Waldhauser, Felix; Ellsworth, W. L., 2000, A double-difference earthquake location algorithm—Method and application to the northern Hayward fault: Bulletin of the Seismological Society of America, v. 90, no. 6, p. 1353-1368.

Wintle, A. G.; Murray, A. S., 2006, A review of quartz optically stimulated luminescence characteristics and their relevance in single-aliquot regeneration dating protocols: Radiation Measurements, v. 41, issue 4, p. 369-391.

Wyss, Max; Wiemer, Stefan; Zuniga, Ramon, 2001, ZMAP—A tool for analyses of seismicity patterns: [Published by authors], 57 p. [http://www.earthquake.ethz.ch/software/zmap/cookbook.pdf].

Appendix 1. Radiocarbon ages in the Monroe 7.5-minute quadrangle and the easternmost part of the adjacent Maltby 7.5-minute quadrangle

Radiocarbon ages in the Monroe 7.5-minute quadrangle and the easternmost part of the adjacent Maltby 7.5-minute quadrangle. For sample locations, see 'age sites' on the map sheet of Dragovich and others (2011) or the provided latitude and longitude. Lab uncertainty values are one standard deviation (68% confidence interval) and include random errors that can be estimated by the lab but exclude uncertainties that cannot be detected by the laboratory's analytical procedures. Analyses were performed by Beta Analytic, Inc. (Miami, Florida). Conventional radiocarbon ages are adjusted for measured $^{13}C/^{12}C$ ratio. 'yr B.P.' signifies radiocarbon years before A.D.1950. Sand geochemical, petrographic, provenance, IRSL and OSL age, and other information are collected for many of the radiocarbon sites (Table 1). *Geologic units*: unit Qc_{ol}: Olympia beds, local provenance (Pleistocene); unit Qc_{o}: Olympia beds, Skykomish River provenance (SP) (Pleistocene); unit Qc_{ws}: Whidbey Formation, Snoqualmie or Skykomish River provenance (Pleistocene); unit Qc_{pf}: nonglacial deposits, Snoqualmie River or Skykomish River provenance, undivided (Pleistocene). We report only the radiocarbon ages that are in or very near the quadrangle. See Dragovich and others (2007) for a compilation of radiocarbon sites in the Fall City quadrangle south of the map area; also see Dragovich and others (2009b, 2010b) for a compilation of radiocarbon sites in the Snoqualmie and Carnation quadrangles south of the present map area, respectively. See Sherrod and others (2008) for radiocarbon ages from fault trenches in the Redmond and Maltby quadrangles west of the Monroe quadrangle. Data below organized chronologically from youngest to 'infinite' radiocarbon ages. AMS, radiocarbon analysis by atomic mass spectrometry for small samples; IRSL, infrared-stimulated luminescence sediment dating technique; OSL, optically stimulated luminescence sediment dating technique; EB, exploration boring; SP, Snoqualmie or Skykomish River provenance for ancient nonglacial sands. All elevations are measured above mean sea level.

Boring or site no.	Analyzed organic material (geologic unit)	Measured radio-carbon age	$^{13}C/^{12}C$ (o/oo)	Conven-tional radio-carbon age	Notes, references, and geologic unit
10-56A #2	peat (unit Qc_{o})	17,600 ± 80 yr B.P.	-31.3	17,500 ± 80 yr B.P.	Peat sample from site 56A. Standard radiometric with extended counting. Latitude and longitude are 47.858016 and -121.957805. See notes for 10-56A #1 below for additional information. See photo for site 56A on p. 58.
10-50H	plant material (unit Qc_{o})	18,810 ± 110 yr B.P.	-29.6	18,730 ± 110 yr B.P.	Nonglacial micaceous sand, silt, silty clay, and pebbly sand with disseminated dark organic material, including plant material and flattened sticks, in cutbank outcrop along Woods Creek (~20 ft above creek). Stratigraphically and compositionally similar to nearby site 56A. Standard radiometric analyses with extended counting. Latitude and longitude are 47.860855 and -121.955319. See photo 50H on p. 55.
10-56A #1	wood from peat (unit Qc_{o})	19,930 ± 130 yr B.P.	-25.1	19,920 ± 130 yr B.P.	Nonglacial SP stratified micaceous sand, silt, and peat well exposed in a Woods Creek cutbank a few hundred feet southeast of the motel. Sands are crossbedded, and locally sands and silts are liquefied. Also see sample 10-50H north of this site. Age likely more representative than 10-56A #1 because small sticks and twigs from the sample were carefully separated from the peat in the lab and cleaned under the microscope in an effort to eliminate contamination by modern organics. Standard radiometric with extended counting. We petrographically analyzed a medium to fine sand near the peat. This SP sand contains ~20 % monocrystalline quartz and lesser but distinct plagioclase, potassium feldspar, hornblende, biotite, and granitic lithic grains (some granitic grains contain internal potassium feldspar, ± biotite and hornblende); most lithics are granitic but contains a few meta-argillite and volcanic grains. Latitude and longitude are 47.858016 and -121.957805. See photo for site 56A on p. 58.
OW-8	Organic sediment (unit Qc_{ol})	23,100 ± 110 yr B.P.	-25.6	23,090 ± 110 yr B.P.	Sample from geotechnical boring OW-8 by Associated Earth Sciences (1999) on Cougar Ridge. Because sample was obtained from a deep geotechnical boring at a depth of 75 ft below the surface, the chance of contamination by modern organics is minimal, and thus the sample was not microscopically cleaned prior to AMS analysis by Beta Analytic, Inc. Beta Analytic obtained 5.3 mg of charred or heated plant material from the bulk sediment sample. Sands sampled from unit Qc_{ol} in boreholes on Cougar Ridge have a local provenance and contain significant lithic mélange belt metamorphic and Tertiary volcanic provenance, including metasandstone, meta-argillite and greenstone clasts. See 'age site OW-8' on map sheet of Dragovich and others (2011) for location.

Boring or site no.	Analyzed organic material (geologic unit)	Measured radio-carbon age	$^{13}C/^{12}C$ (o/oo)	Conven-tional radio-carbon age	Notes, references, and geologic unit
10-49E	plant material (unit Qc_O)	24,820 ± 170 yr B.P.	-27.1	24,790 ± 170 yr B.P.	Nonglacial sands, silts, and organic silt with disseminated dark organic material, including plant material and charcoal in cutbank outcrop along Skykomish River below eastern end of parking lot to trailer park. Outcrop extends into the river and below summer water level and is undergoing active bank erosion. A silty fine sand near the radiocarbon sample is monocrystalline quartz-rich with lesser but significant plagioclase, biotite, hornblende, and potassium feldspar and distinct SP batholith provenance. Sample microscopically cleaned before sending to Beta Analytic for AMS analyses. Latitude and longitude are 47.845773 and -121.873481. See photo for site 49E on p. 54.
OW-5	Plant material (unit Qc_{ol})	38,700 ± 390 yr B.P.	-27.5	38,660 ± 390 yr B.P.	Sample from geotechnical boring EB-5 by Associated Earth Sciences (1999) on Cougar Ridge. Sample OW-5 obtained from nonglacial gray sandy silt with occasional wood fragments at a drilling depth of 35 ft. Because the sample was obtained from a deep geotechnical boring, the chance of contamination by modern organics is minimal and thus the sample was not microscopically cleaned prior to AMS analysis by Beta Analytic. Beta Analytic obtained 6.8 mg of uncharred plant material from the bulk drilling sediment sample. Sands sampled from unit Qc_{ol} in boreholes on Cougar Ridge have a local provenance and contain significant lithic mélange belt metamorphic and Tertiary volcanic provenance, including metasandstone, meta-argillite, and greenstone clasts. See age site OW-5 on map sheet of Dragovich and others (2011) for location.
10-22A	peat (unit Qc_{ws})	40,000 ± 350 yr B.P.	-25.1	40,000 ± 350 yr B.P.	Thick, crossbedded ancient SP nonglacial sands and pebbly sands with disseminated dark organic material, including plant material, overlain by Vashon advance outwash and Vashon till in the Cadman High Rock quarry on the western SE highlands. Well exposed crossbedded fluvial sediments in 50 ft high active pit cutbank. The finite age (40,000 yr B.P.) is interpreted to be erroneous and the result of contamination by modern organics as a result of the ages of nearby OSL samples 25A and 25B from the same active quarry cutbank strata (OSL ages 101 ± 4.47 ka and 107 ± 9.87 ka at age sites 25A and 25B) and the infinite radiocarbon age at nearby site 25A (below). Sample contained minor rootlets that were microscopically removed prior to sending to laboratory. We suspect that the minor contamination from unseen modern rootlets in the analyzed AMS sample led to the finite age. See sand composition at nearby 'infinite' radiocarbon sample 25A. Sample elevation is 410 ft at latitude and longitude 47.813058 and -121.964654. See photo for site 22A on p. 43.
10-24D	Charred organics (unit Qc_O)	NA	-24.9	>43,500 yr B.P.	Nonglacial crossbedded and plane-bedded sands with stringers of disseminated dark organic material in a 30-ft-high large road outcrop. Bedded fluvial channel gravels dominate the uppermost part of the outcrop. The few modern rootlets in the sample were removed microscopically prior to submission of sample to Beta Analytic for AMS analysis. We obtained an IRSL age of ~51,500 yr B.P. a meter from radiocarbon age sample 10-24D. Coarse sands at the site contain significant monocrystalline quartz sand with distinct granitic lithics with some metamorphic and sedimentary lithics; monocrystalline quartz is significantly higher than poly-crystalline quartz, suggesting a nonglacial SP provenance, and is petrographically very similar to modern Skykomish alluvium, which also contains significant monocrystalline quartz, plagioclase, potassium feldspar, and minor but significant hornblende and mica. Other analyzed sands contain a higher percentage of more diverse lithic grain types and contain slightly more serpentinite, metasedimentary lithic clasts, and polycrystalline quartz, suggestive of mixing of ancient Skykomish River alluvium with alluvium derived from the Western mélange belt to the east. We suspect these beds incorporated older Quaternary sediment as the ancient Skykomish River incorporated emerging local highlands detritus. Latitude and longitude are 47.844443 and -121.881831. See photo for site 24D on p. 47.
10-25A	charred organics and charcoal (Qc_{ws})	NA	-25.0	>43,500 yr B.P.	Well exposed crossbedded ancient SP sands and pebbly sands that underlie advance outwash in the Cadman High Rock quarry on the western SE highlands. Radiocarbon sample taken at same stratigraphic level (elevation ~403 ft) as and within meters of two OSL samples (ages 101 ± 4.47 ka and 107 ± 9.87 ka at age sites 25A and 25B, respectively; also see radiocarbon site 22A). This AMS sample was microscopically cleaned prior to sending to Beta Analytic. SP sands at the site petrographically contain ~20% monocrystalline quartz with lesser but significant plagioclase, hornblende, potassium feldspar, and variable lithics, including significant granitic lithics; some granitic lithics contain internal potassium feldspar indicating a 'true granite' SP batholith provenance. Latitude and longitude are 47.814139 and -121.963134. See photo for site 25A on p. 48.

Boring or site no.	Analyzed organic material (geologic unit)	Measured radio-carbon age	$^{13}C/^{12}C$ (o/oo)	Conven-tional radio-carbon age	Notes, references, and geologic unit
10-28D	charred organics (unit Qc_{pf})	NA	-24.0	>43,500 yr B.P.	Site 28D is from a 2–4 m-high river cutbank along the Snoqualmie River in the Maltby quadrangle. AMS sample microscopically cleaned of many fine modern rootlets prior to sending to Beta Analytic. Petrographically, sands at the site contain significant monocrystalline quartz with lesser but significant plagioclase, hornblende, granitic lithic grains, and potassium feldspar; also contain other variable lithic grains; distinct SP composition. The silts and sands at this site are intensely liquefied, folded as well as fractured. We suspect these deposits were deformed by Quaternary offset along the Cherry Creek fault, which projects to near this site and appears to align with fault scarps and lineaments mapped by Sherrod and others (2008) along the southwestern slopes of Lords Hill in the western Maltby 7.5-minute quadrangle. Latitude and longitude are 47.805664 and -121.003901. See photo for site 25A on p. 48.

Appendix 2. Geochemical data

See a2_geochemical_data_monroe.xls

Appendix 3. Geochemical sample locations

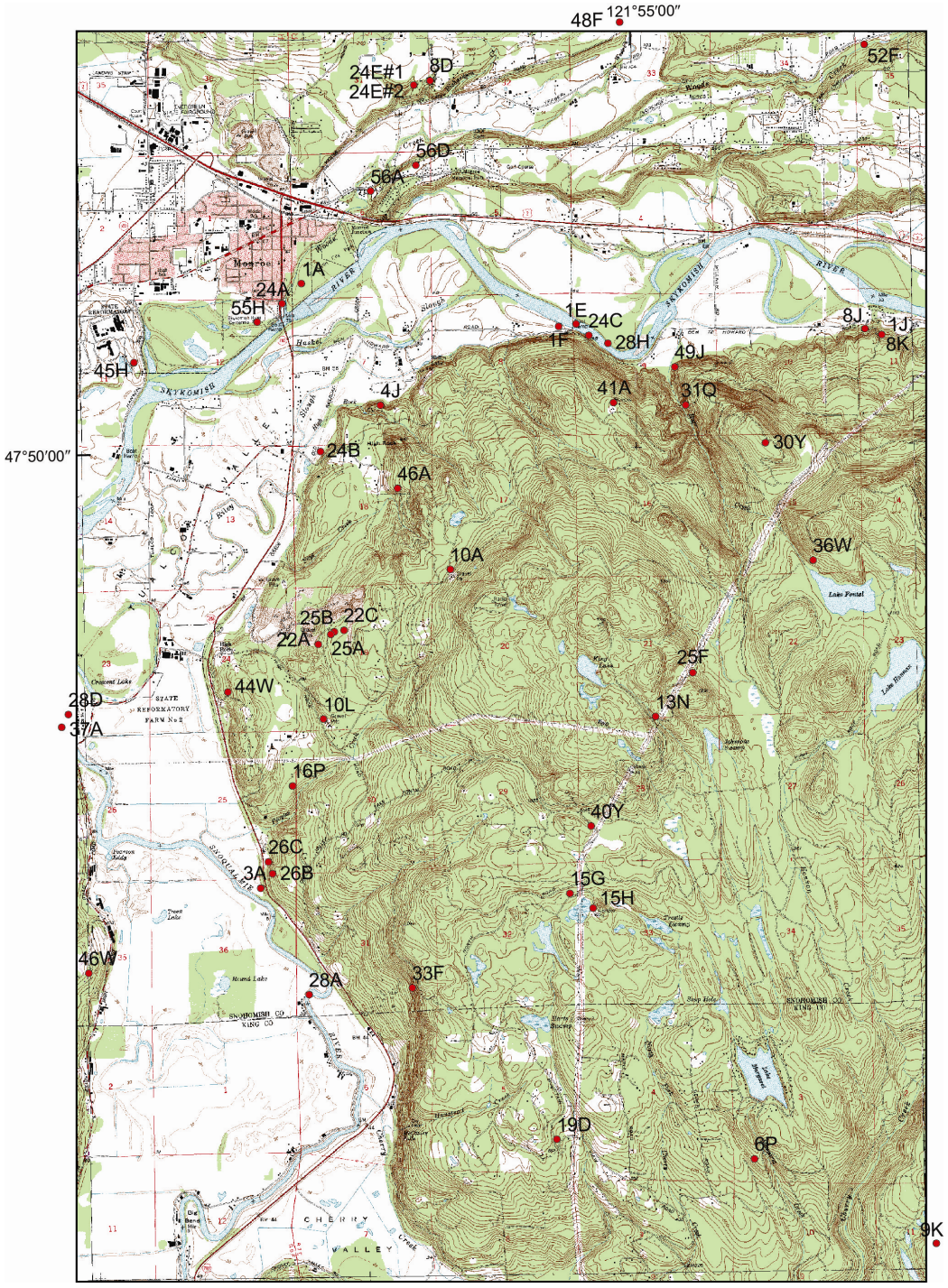

Appendix 4. Additional geochemical plots

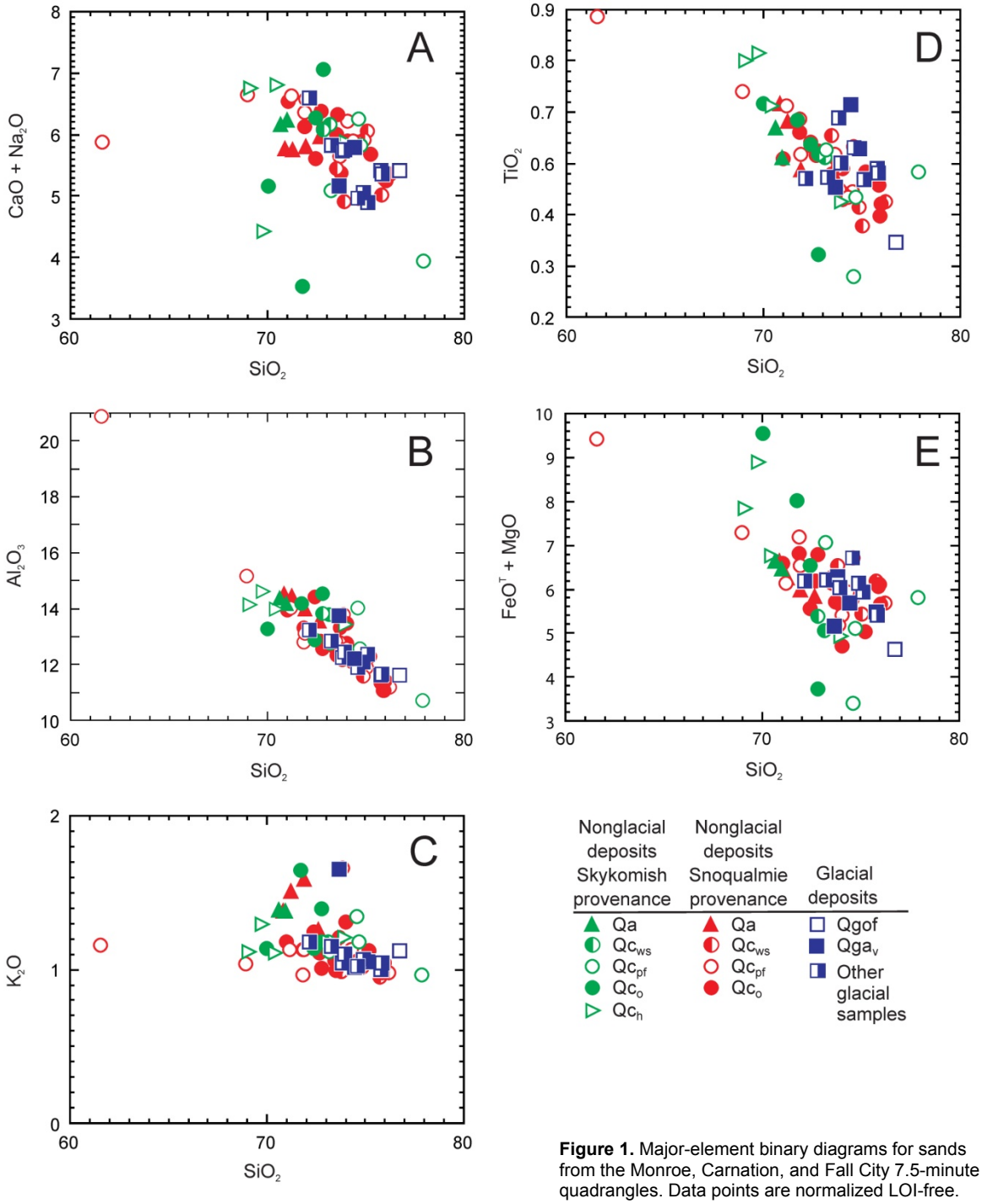

Figure 1. Major-element binary diagrams for sands from the Monroe, Carnation, and Fall City 7.5-minute quadrangles. Data points are normalized LOI-free. **A.** $CaO+Na_2O$ vs. SiO_2. **B.** Al_2O_3 vs. SiO_2. **C.** K_2O vs. SiO_2. **D.** TiO_2 vs. SiO_2. **E.** $FeO+MgO$ vs. SiO_2.

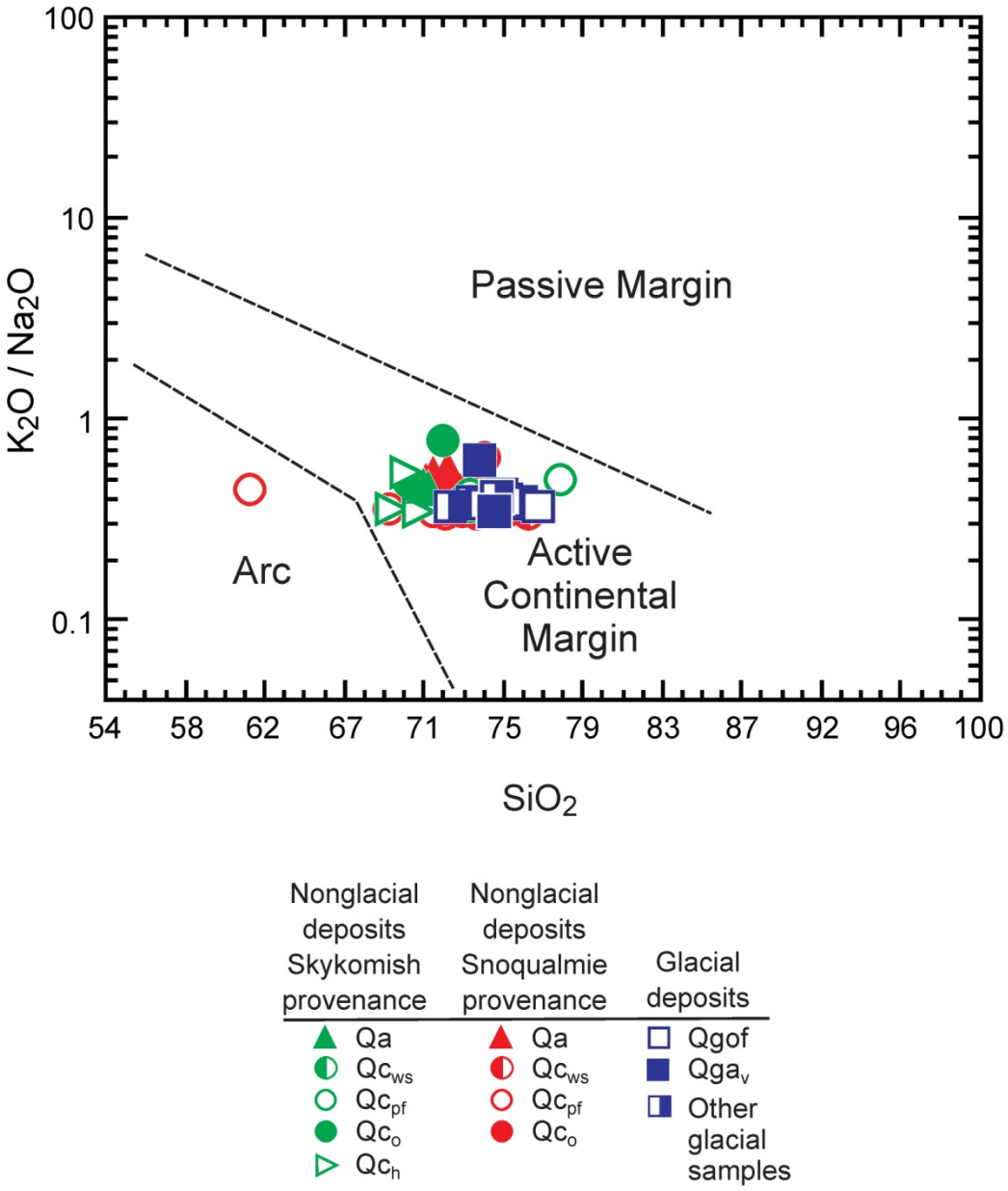

Figure 2. Sands from the Monroe, Carnation, and Fall City 7.5-minute quadrangles plotted on the log K_2O/Na_2O vs. SiO_2 tectonic discrimination diagram of Roser and Korsch (1986). Data normalized LOI-free before plotted.

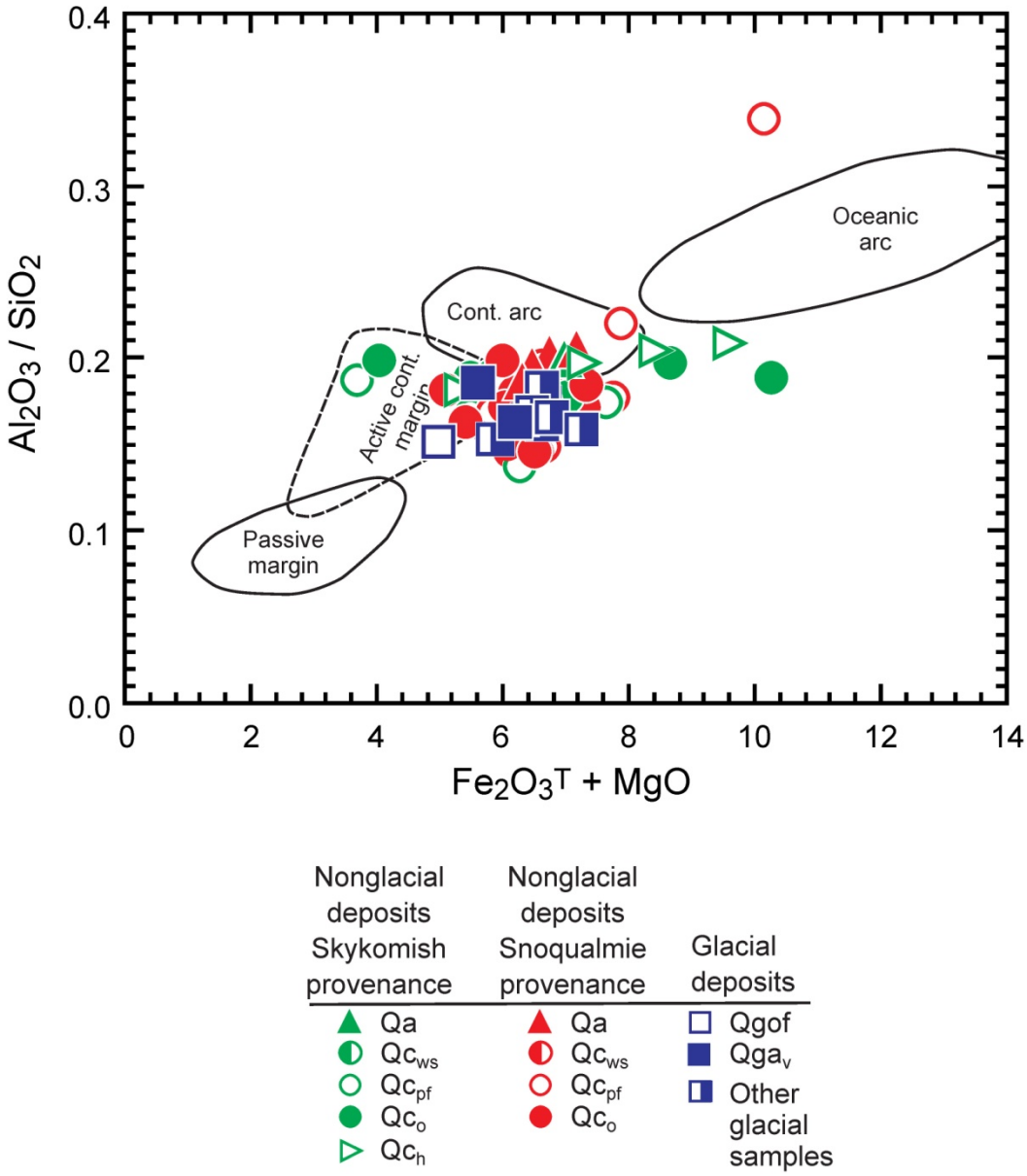

Figure 3. Sands from the Monroe, Carnation, and Fall City 7.5-minute quadrangles plotted on the Al_2O_3/SiO_2 vs. $Fe_2O_3^T$ + MgO sandstone tectonic discriminant diagram of Bhatia (1983). Data normalized LOI-free before plotted.

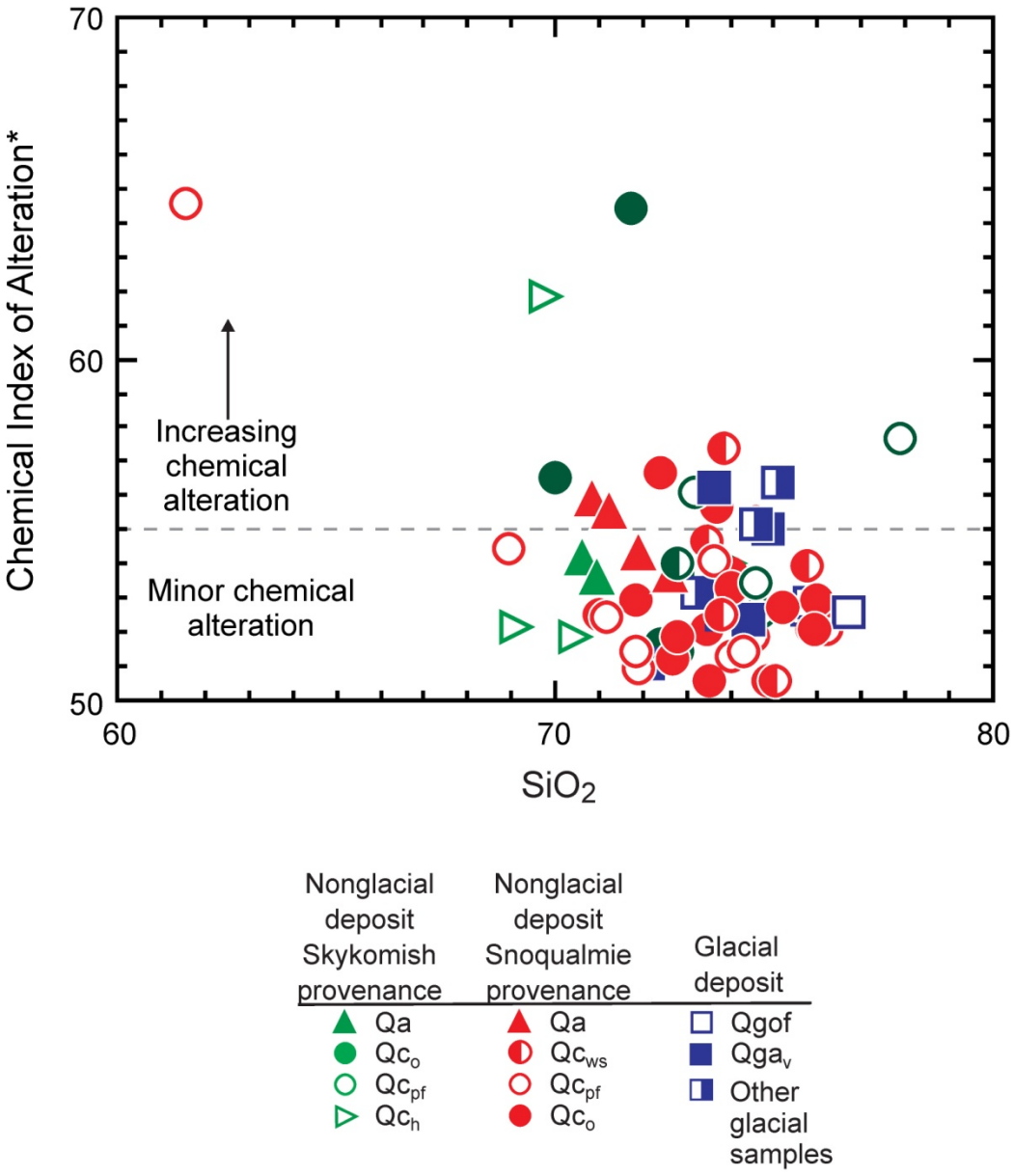

Figure 4. Chemical index of alteration vs. SiO_2 for sands from the Monroe, Carnation, and Fall City 7.5-minute quadrangles. Chemical index of alteration from Nesbitt and Young (1989) and Nesbitt (2003). Data normalized LOI-free before plotted.

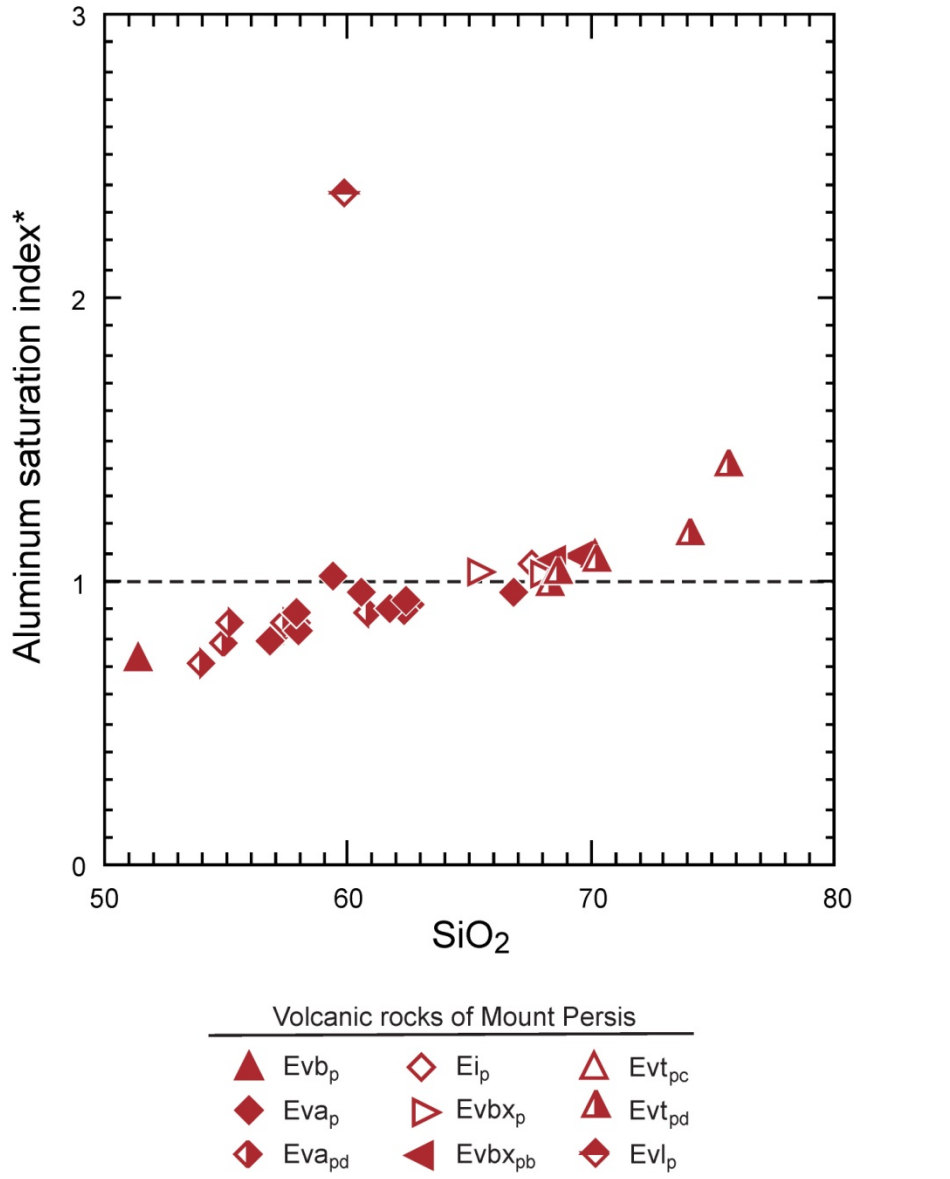

Figure 5. Aluminum saturation index vs. SiO_2 diagram for volcanic rocks of Mount Persis of Tabor and others (1993). Samples are from Monroe, Carnation, and Snoqualmie 7.5-minute quadrangles. Aluminum saturation index calculated using the method of Frost and others (2001). Data normalized LOI-free before plotted.

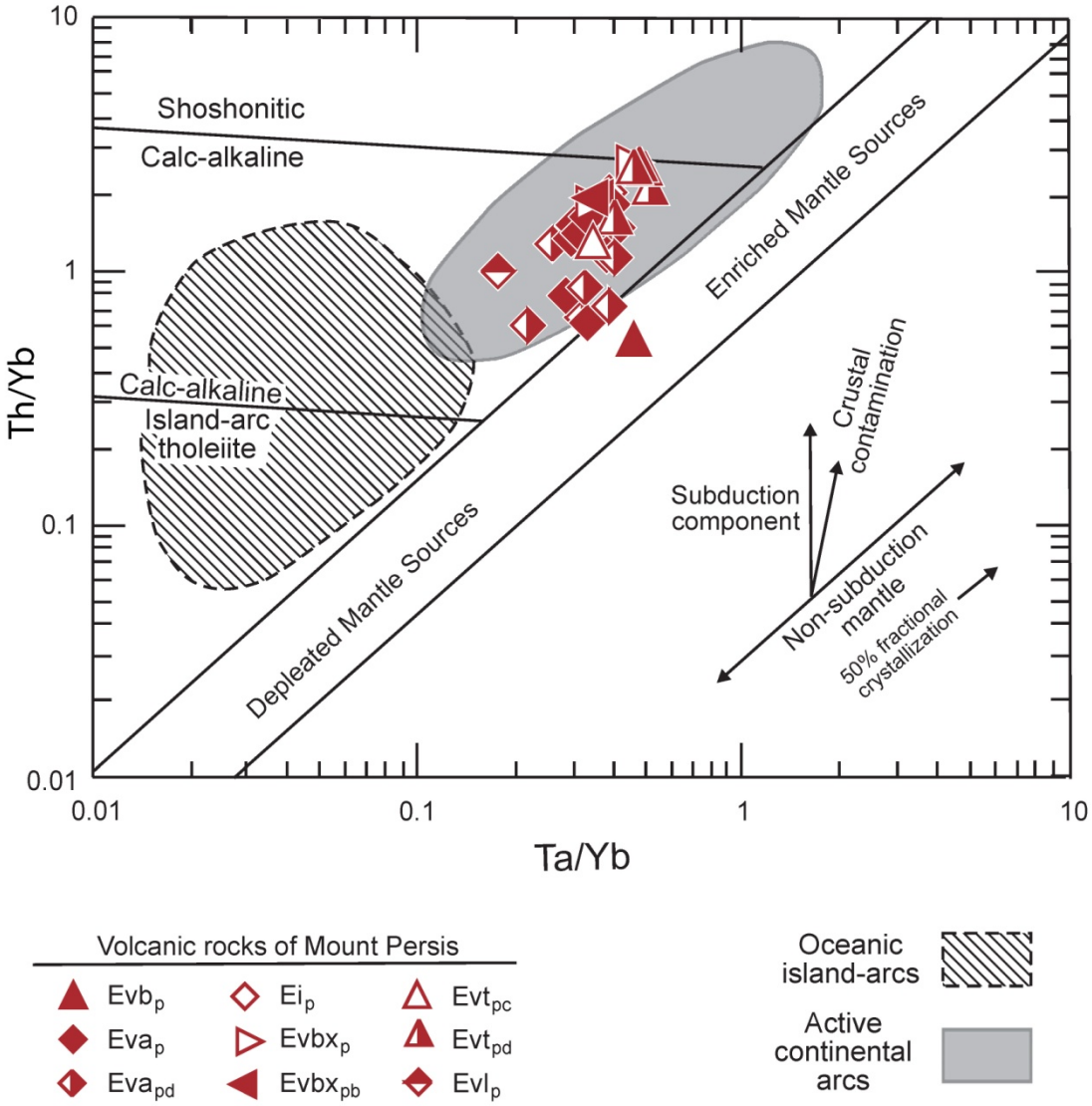

Figure 6. Th/Yb vs.Ta/Yb discrimination diagram for volcanic rocks of Mount Persis of Tabor and others (1993). Samples are from Monroe, Carnation, and Snoqualmie 7.5-minute quadrangles. Diagram after Pearce (1982, 1983). Data normalized LOI-free before plotted.

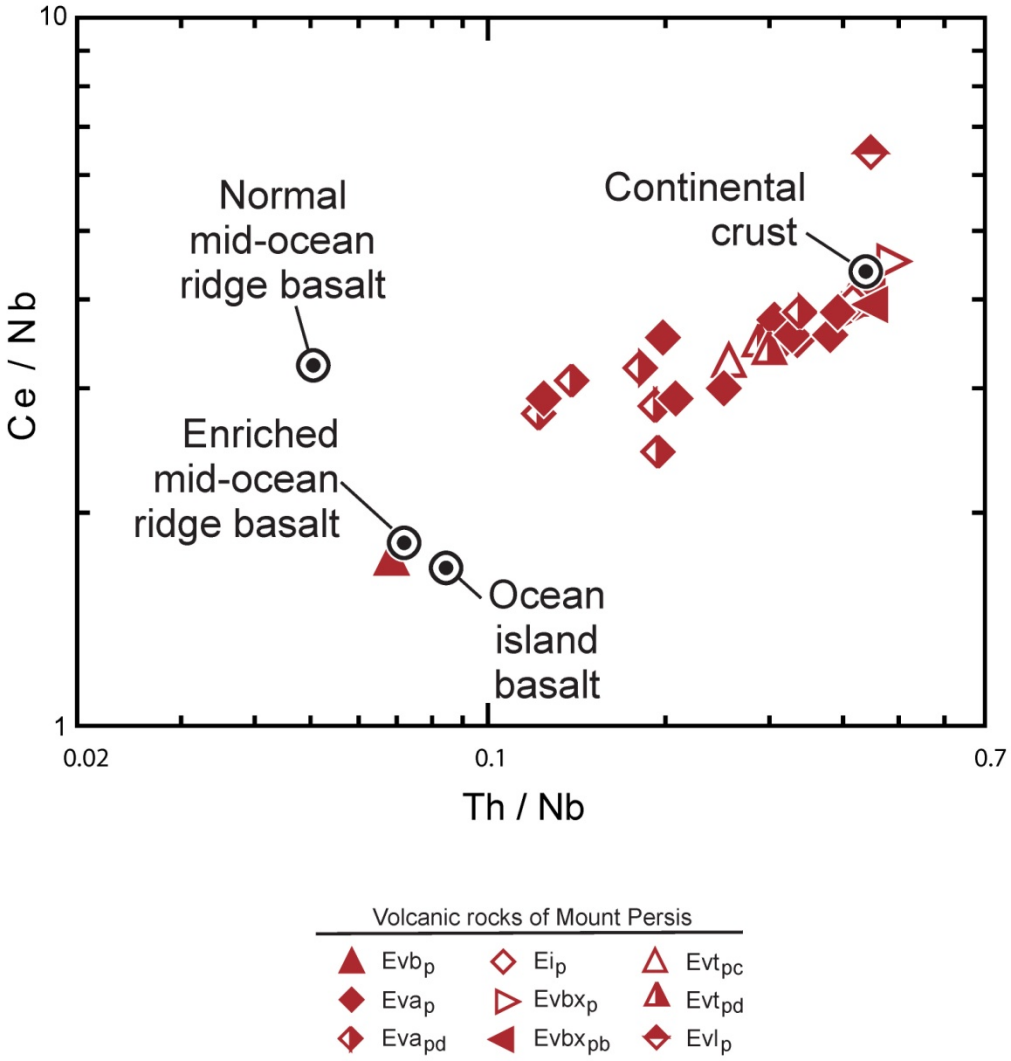

Figure 7. Ce/Nb vs.Th/Nb diagram for volcanic rocks of Mount Persis of Tabor and others (1993). Samples are from Monroe, Carnation, and Snoqualmie 7.5-minute quadrangles. Diagram modified from Saunders and others (1988). Ocean island basalt and normal and enriched mid-ocean ridge basalt values are from Sun and McDonough (1989). Average value of continental crust is from McLennan (2001). Data normalized LOI-free before plotted.

Appendix 5. U/Pb geochronology

See a2_geochemcial_data_monroe.xls.

Appendix 6. Geophysical map, expanded geophysical cross section, and table of rock physical properties

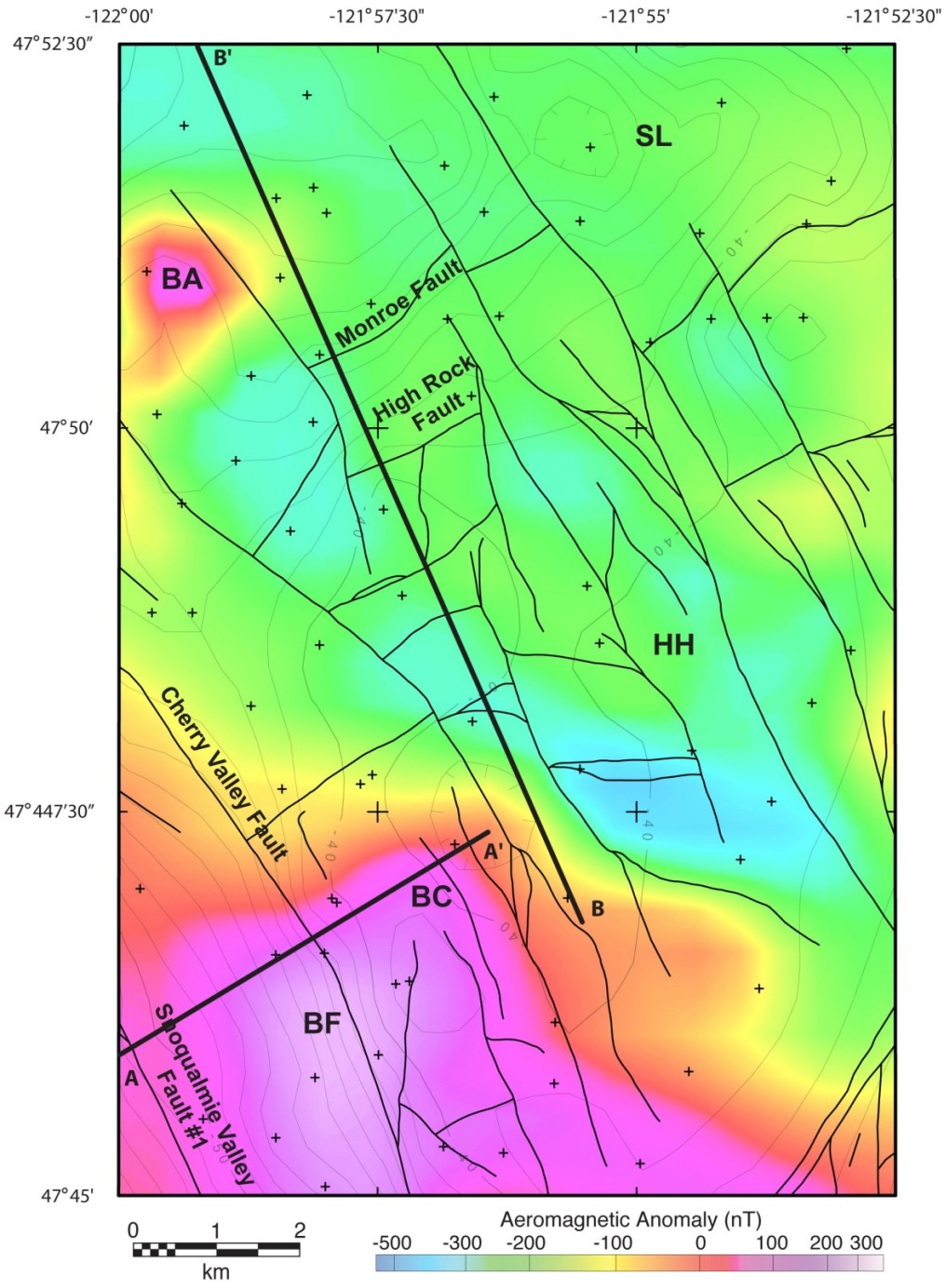

Figure A. Geophysical map of the Monroe quadrangle. Base map is the reduced-to-pole aeromagnetic anomaly map; the reduce-to-pole filter centers magnetic highs over their source bodies. Isostatic gravity contours (1 mGal interval) are labeled in mGals, with closed lows indicated by hachures. Darker lines are faults from Dragovich and others (2011). Crosses indicate locations of gravity measurements controlling the isostatic gravity grid. Cross sections A–A′ and B–B′ coincide with structural cross sections A and B in Dragovich and others (2011). Selected faults are labeled. BA, basalt outcrop; BC, interpreted channelized basalts; BF, basalt flows buried on the edge of the Seattle basin; HH, gravity high over the topographic highlands; SL, gravity low associated with the Skykomish River basin.

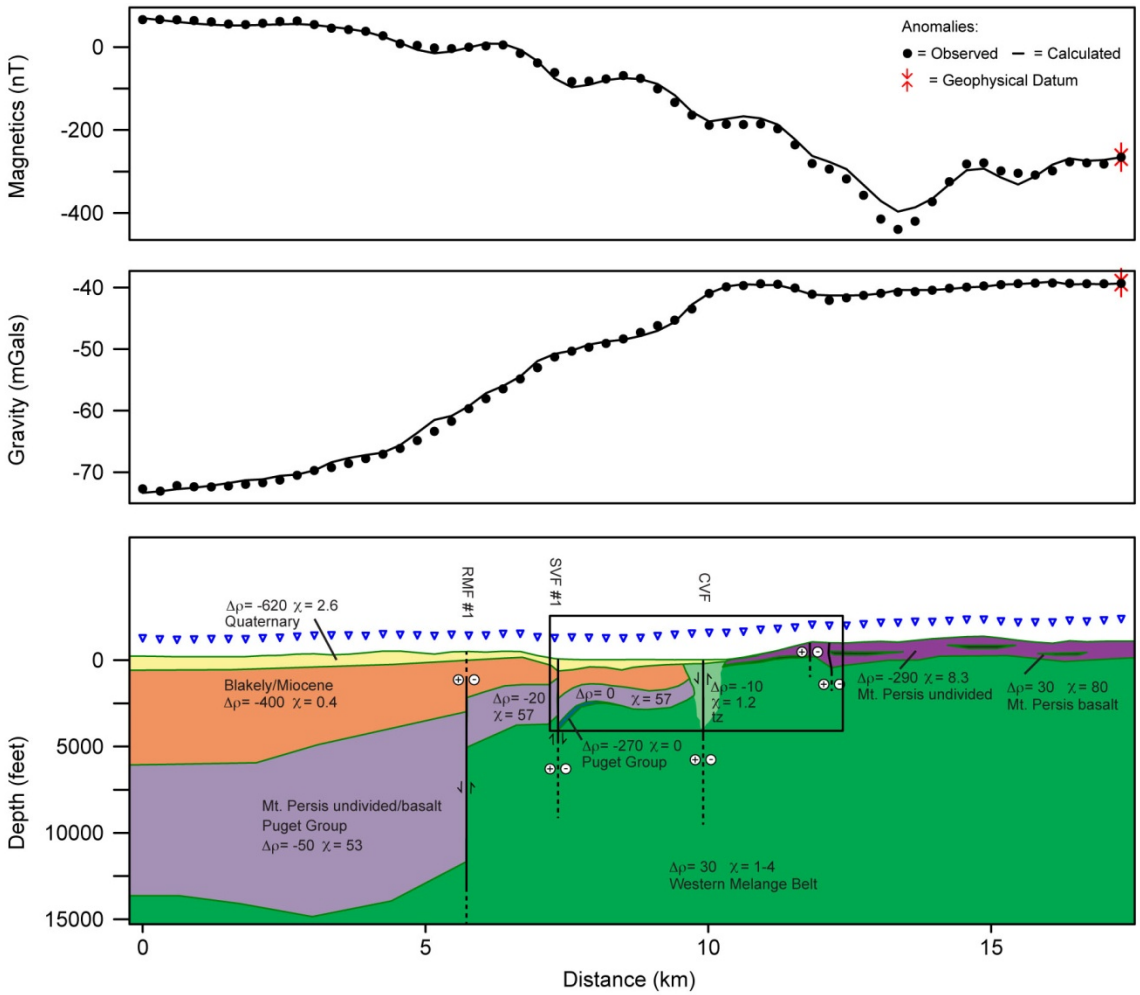

Figure B. Match of predicted gravity and aeromagnetic anomalies to data from the region, no vertical exaggeration. The expanded cross section above is located along Cross Section A–A′ (Figure A), but is longer in length. Model A (Dragovich and others, 2011) is inside the outlined box. The model is assumed to extend to infinity in both directions perpendicular to the profile. The blue triangles in the lower panel indicate the height of the flight line above the ground for the aeromagnetic data. $\Delta\rho$ is the density contrast relative to normal crust (2670) in kg/m^3; χ is magnetic susceptibility in SI units multiplied by 1000. Solid lines show fault locations that are well-controlled by the geophysical or geologic data. Dotted lines show fault locations that are controlled by geologic mapping at the surface and (or) geophysical anomalies, but are less certain at depth. RMF, Rattlesnake Mountain fault; SVF, Snoqualmie Valley fault; CVF, Cherry Valley fault. Although not separated, the Puget Group likely extends west of SVF1 and underlies or interfingers with the volcanic rocks of Mount Persis. Blakeley, Blakeley Formation; Miocene, undivided Miocene sedimentary and volcanic rocks (Dragovich and others, 2011).

Geologic Unit	SBD	95%	SH	95%	NH	SO	95%	NO
Blakeley Formation, OE	2.27	0.24	1.1	0.6	5	0.4	0.1	78
Puget Group (undivided)	2.48	0.04	4.4	1.8	62	7.2	0.9	531
Miocene sedimentary and volcanic rocks (undivided)	1.85	0.29	1.5	0.3	4	1.9	0.1	30
Mt. Persis (undivided)	2.52	0.06	7.9	2.4	25	9.9	0.8	331
Mt. Persis andesite, Eva_p	2.63	0.02	12.6	2.5	9	11.2	1.3	131
Mt. Persis basaltic andesite, Eva_{pd}	2.70	0.02	15.2	1.4	3	17.3	1.3	71
Mt. Persis breccia, $Evbx_p$	2.43	0.05	4.2	3.0	6	6.1	0.8	62
Mt. Persis volcanic sedimentary rocks, Evc_p	2.26	0.12	4.2	2.3	3	7.4	1.1	8
Mt. Persis tuff, Evt_p	2.15		1.8		1	2.1	0.5	59
Western mélange belt (undivided)	2.70	0.05	4.0	6.0	30	6.4	1.4	242
Quaternary units (undivided), Q	2.01	0.16	5.2	6.8	6	2.6	0.1	575
cataclasite, tz						1.2	0.6	35

Figure C. Table of physical property values for rocks exposed on the Monroe quadrangle. SBD, saturated bulk density in grams/cubic centimeter from hand sample; 95%, 95% confidence interval; SH, susceptibility from hand sample in SI x 10^3; NH, number of hand samples; SO, susceptibility from outcrop measurements in SI x 10^3; NO, number of outcrop measurements; Mt. Persis, volcanic rocks of Mount Persis of Tabor and others (1993). Unit OE is ΦE_c and ΦEn of Dragovich and others (2011); Puget Group is unit Evs_{pg} of Dragovich and others (2011); the undivided Miocene unit is unit Mvc of Dragovich and others (2011); undivided Mt. Persis is unit Evs_p of Dragovich and others (2011); Western mélange belt is unit KJm of Dragovich and others (2011); undivided Quaternary is all the units starting with 'Q' of Dragovich and others (2011); cataclasites are units tz, tz, and Qtz of Dragovich and others (2011).

Appendix 7. Photos of selected Quaternary liquefaction, structural, and stratigraphic features

Unfortunately, due to the quality of the outcrops, dense vegetation, and locally poor lighting conditions, only a few of the structural and stratigraphic features we observed in the field are presented here. Photos are by Julia Labadie. Abbreviations used here include: AMS, radiocarbon analysis by atomic mass spectrometry for small samples; IRSL, infrared-stimulated luminescence sediment dating technique; OSL, optically stimulated luminescence sediment dating technique; SP, Snoqualmie or Skykomish River provenance for ancient nonglacial sands. Sand geochemical, petrographic, provenance, IRSL/OSL and radiocarbon age, and other information were collected for some of these sites (Table 1). Some of the locations illustrated below are 'significant sites' on the map sheet of Dragovich and others (2011).

Site 17H, Photo 1593

Mildly cataclastically deformed plagioclase-rich andesites (mapped as unit tz) close to Highway 203 in the southern part of the Monroe quadrangle. These cataclasites occur along the western end of the Fontal Road fault and are within shear zones that strike 110 to 222° and dip 28 to 90°. Shown here is a less deformed andesite body within intensely sheared and fractured cataclasite of the Fontal Road reverse fault. (See map sheet in Dragovich and others, 2011.)

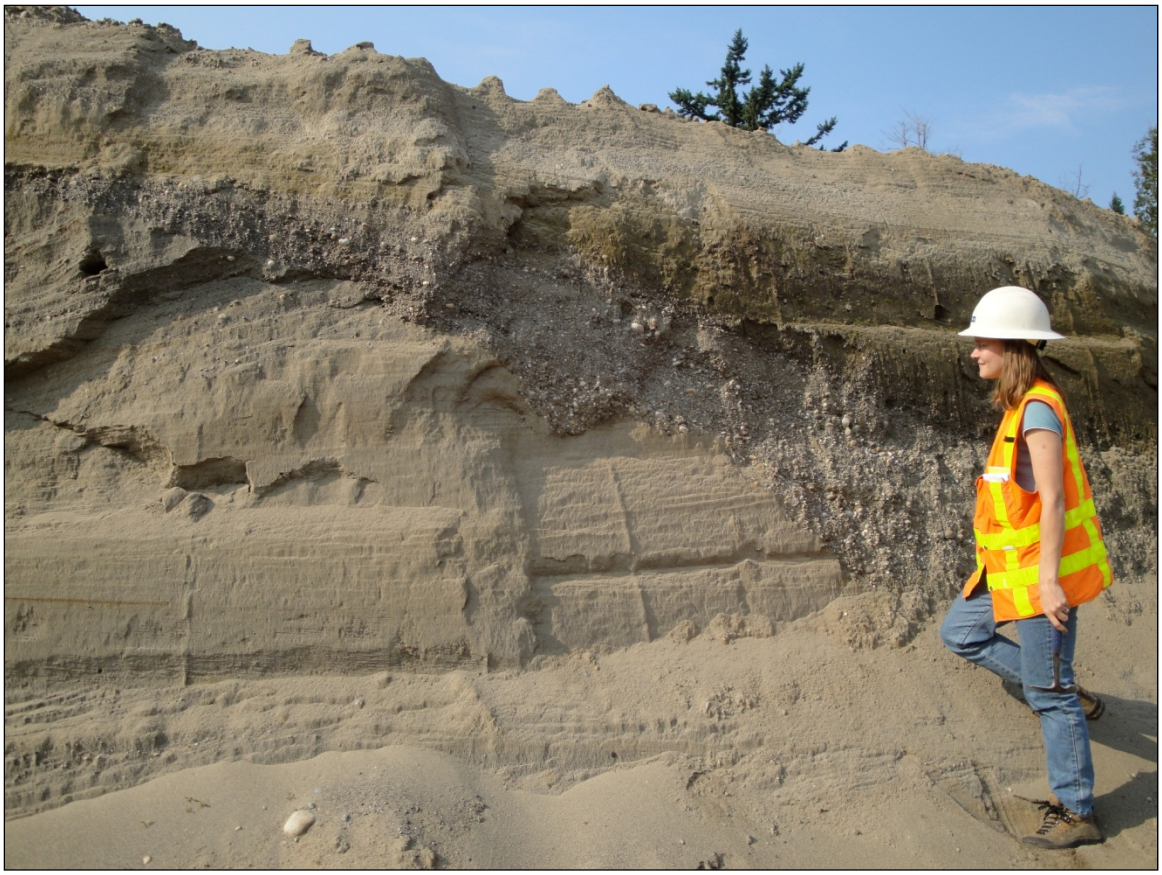

Radiocarbon Age Site 22A, Photo 1632

Whidbey Formation (unit Qc_{ws}), ancient Snoqualmie River–provenance alluvium, in the Cadman Quarry south of Monroe and just north of the Snohomish/King county line. Strata here consist of nonglacial sands and pebbly sands with disseminated organic material including plant debris. These crossbedded fluvial sediments are exposed along a 50-ft-high active quarry wall, where they are overlain by younger Vashon advance outwash and Vashon till. (Photo shows a shorter pit wall.) Petrographically, sediments directly to the south of this site contain grains of plagioclase, quartz, biotite, and lithic fragments of greenstone, volcanics, and minor granite; presence of a gravel-rich dike suggests liquefaction. Low content of monocrystalline quartz with high content of polycrystalline quartz and lithics including serpentine and volcanics suggest incorporation of local detritus (Dragovich and others, 2011). OSL-dated sands near the photo have a distinct ancient Snoqualmie provenance, indicating mixing of local and ancient Snoqualmie detritus in these old fluvial deposits. This exposure is elevated (410 ft or 125 m apsl) and has possibly been uplifted by offset along the Cherry Valley and (or) Monroe faults. The finite radiocarbon age (40,000 yr B.P.) is interpreted to be erroneous and the result of contamination by modern organics, because of ages obtained for nearby OSL samples 10-25A and 10-25B from the same active quarry wall (101 ± 4.47 ka and 107 ± 9.87 ka at age sites 25A and 25B) and an infinite radiocarbon age at site 25A. (See radiocarbon age sample 10-22A in Appendix 1 and OSL/IRSL age sample 10-22A in Table 2.) Geologist for scale. (See map sheet in Dragovich and others, 2011.)

Site 22G, Photo 1661

Alteration and brecciation along shears within columnar basaltic andesite (unit Eva_{pd}) in the Cadman Quarry, mapped as unit tz (tectonic zone). Note the subhorizontal volcanic flow columns on the right which indicate subvertical flow bedding. This zone of shearing and fault brecciation is roughly 200 ft thick and part of an east-northeast-trending fault zone that is exposed in the wall of the quarry. Latitude/longitude of site is 47.815461/-121.960041. (See map sheet in Dragovich and others, 2011.)

IRSL/OSL Age Site 24A, Photo 1674

An exposure of Olympia beds (unit Qc_o), pre-Fraser nonglacial deposits, at Lewis Creek Park at the confluence of Woods Creek and the Skykomish River immediately south of Monroe. Strata here consist of compact, thinly bedded, medium sand and silty fine sand, pebbly sand, and gravels containing boudinaged folds and rootless chaotic folds in silty beds as a result of intense sediment liquefaction. This unit locally contains charcoal, disseminated organic matter, trough and ripple crossbedding, graded beds, sand dikes, and chaotic or folded bedding as observed here. Sand clasts suggest predominately granitic source rocks typical of Snoqualmie provenance Tertiary sources, including significant hornblende and plagioclase. (See complete description in Dragovich and others, 2011.) Silt beds at this site strike 122 to 135° and dip 15 to 22°. We obtained an infrared-stimulated luminescence (IRSL) age of 50.5 ±3.53 ka from this site. (See OSL/IRSL age sample 10-24A in Table 2.) (See map sheet in Dragovich and others, 2011.)

IRSL/OSL Age Site 24B, Photo 1371

Distorted, chaotic bedding and rootless folds in the Hamm Creek formation (Qc_h) at an outcrop on N. High Rock Road. Strata here consist of compact laminated silts with sandy interbeds, exhibiting intense liquefaction features. This unit is composed of pre-Fraser nonglacial deposits and ancient Snoqualmie River alluvium that contains significant monocrystalline quartz (Table 3). We obtained an IRSL age of 233 ±10.9 ka (~233,000 yrs B.P.) at this site (see age site 10-24B in Table 2), indicating a correlation with the Hamm Creek formation. Similar intense liquefaction is evident to the southeast of site 24B at site 46A (also assigned to unit Qc_h). Quaternary bedding measurements suggest that the unit is tilted to the north and likely broadly folded south of the Monroe fault (Dragovich and others, 2011). (See map sheet in Dragovich and others, 2011.)

IRSL/OSL and Radiocarbon Age Site 24D, Photo 1447

Olympia beds (unit Qc_O) exposed on 260th Ave SE, Monroe quadrangle (latitude/longitude 47.844443/-121.881831). Strata here consist of nonglacial crossbedded and plane-bedded sands with stringers of disseminated dark organic material in a 30-ft-high roadside outcrop. Bedded fluvial channel gravels dominate the uppermost part of the exposure. Coarse sands at the site petrographically contain significant monocrystalline quartz sand with distinct granitic lithics with some metamorphic and sedimentary lithics; monocrystalline quartz is significantly higher than polycrystalline quartz, suggesting a nonglacial SP provenance petrographically similar to modern Skykomish alluvium. Other analyzed sands contain a higher percentage of more diverse lithic grain types and contain slightly more serpentinite, metasedimentary lithic clasts, and polycrystalline quartz, suggestive of mixing of ancient Skykomish River alluvium with alluvium derived from the Western mélange belt to the east (Dragovich and others, 2011). AMS analysis on charred organics by Beta Analytic Inc. indicated an age >43,500 yr B.P. We obtained an IRSL age of ~51,500 yr B.P. a meter away from the radiocarbon sample site. (See radiocarbon age sample 10-24D in Appendix 1 and OSL/IRSL age sample 10-24D in Table 2.) (See map sheet in Dragovich and others, 2011.)

IRSL/OSL and Radiocarbon Age Site 25A, Photo 1807

Well-exposed and massively crossbedded ancient SP sands and pebbly sands (unit Qc_{ws}, Whidbey Formation) that underlie advance outwash in the Cadman Quarry on the western SE highlands near the Snohomish/King county border. SP strata here consist of light brownish-gray medium-fine sand to pebbly sand and minor organics and charcoal. Sands contain hornblende, plagioclase, and lithics, some granitic and suggestive of a graded batholithic provenance. Significant amounts of potassium feldspar are also present (Dragovich and others, 2011). We correlate these strata with the Whidbey Formation (~80,000–130,000 yr B.P.) on the basis of age, composition, and stratigraphic position. A sample for radiocarbon dating was taken within meters of two OSL samples (25A and 25B; 101 ± 4.47 ka and 107 ± 9.87 ka). An 'infinite' radiocarbon age (>43,500 yr B.P.) was obtained from charred organics and charcoal. (See radiocarbon age sample 10-25A in Appendix 1 and OSL/IRSL age sample 10-25A.) Latitude/longitude of site is 47.814139/ -121.963134. (See map sheet in Dragovich and others, 2011.)

Significant Site 27C, Photo 1831

Vashon advance glaciolacustrine deposits (unit Qgl_V) by a hairpin turn on upper High Rock Road near Highway 203, south of Monroe and WSW of the Cadman Quarry at significant site 27C of Dragovich and others (2011). Strata here consist of silt, sand, and pebble layers that have been folded, likely as a result of ice shear. The lamination along the fold hinge strikes 215 to 240° and dips 18 to 69°, defining a shallowly plunging fold. The orientation of the fold axis is consistent with a Puget ice shear direction to the southeast (azimuth about 140°). (See map sheet in Dragovich and others, 2011.)

Radiocarbon Age Site 28D, Photo 1857

An exposure of pre-Fraser continental deposits (unit Qc_{pf}), nonglacial Snoqualmie River–provenance ancient alluvium, just outside the Monroe quadrangle about 4.5 mi southwest of the town of Monroe. Exposure is at a 2-to-4 m-high eroded bank adjacent to the Snoqualmie River in the Maltby 7.5-minute quadrangle. Strata at this site consist of light yellowish-brown moderately sorted sand, silty sand, and silt, with some pebbles and disseminated organic matter. The silts and sands at this site are intensely liquefied as well as fractured (Dragovich and others, 2011). We suspect these deposits are deformed by Quaternary offset along the Cherry Creek fault, which projects to near this site and appears to align with fault scarps and lineaments mapped by Sherrod and others (2008) along the southwestern slopes of Lords Hill in the western Maltby 7.5-minute quadrangle. Measured bedding attitudes strike 86 to 230° and dip 14 to 70°. Observed minor faults and shears strike 75 to 86° and dip 38 to 40°. We obtained a radiocarbon age of >43,500 yr B.P. on charred organic debris at this site. (See radiocarbon age sample 10-28D in Appendix 1.) Latitude/longitude of site is 47.805664/ -121.003901.

Site 28D, Photo 1859 (see also description above for Site 28D, Photo 1857)

A second exposure of pre-Fraser continental deposits (unit Qc_{pf}) adjacent to the exposure pictured in Site 28D, Photo 1857 above, in the Maltby quadrangle. This exposure exhibits faulted and distorted sand and silt beds; liquefaction features predominate, including rootless folds and sand dikes. Bedding is locally chaotic. Measured fold limbs like those pictured above strike 274 to 312° and dip 29 to 85°. A nearby sand dike (not pictured) strikes 85° and dips 60°. (See map sheet in Dragovich and others, 2011.)

Site 34Y, Photo 1943

Volcanic rocks of Mount Persis (unit Eva_p) exposed in an andesite quarry about a mile east of the Cadman High Rock Quarry. Vesicular andesite flows and flow breccias are sheared and brecciated along a generally northwest-trending fault. Fault brecciation, weak mineralization, and slickensides are visible above. Measured shears strike/dip 60°/70°, 232°/70°, and 53°/66°. (See map sheet in Dragovich and others, 2011.)

Site 48F, Photo 2098

Pre-Fraser nonglacial ancient alluvium (unit Qc_{ws}, Whidbey Formation) exposed on Woods Creek Road near the northern edge of the Monroe quadrangle. Strata here consist of finely laminated beds of light yellowish-brown to orange micaceous silt and sand containing monocrystalline quartz, potassium feldspar, plagioclase, significant granitic lithics, metamorphic lithics, and minor hornblende and pyroxene. A degraded batholithic source provenance is apparent. A more complete petrographic description of this unit can be found in Dragovich and others (2011). Beds strike 30 to 50° and dip 3 to 4° SE. (See map sheet in Dragovich and others, 2011.)

Radiocarbon Age Site 49E, Photo 2119

An exposure of Olympia beds (unit Qc_O), Skykomish River-provenance alluvium, on the bank of the Skykomish River just upstream from the eastern boundary of the Monroe quadrangle. The outcrop extends into the river and below summer water levels and is currently subject to active bank erosion. Strata here consist of nonglacial pale yellow sand and silt with disseminated dark organic material including plant detritus and charcoal. Sediments are micaceous with abundant biotite, monocrystalline quartz, potassium feldspar, and hornblende. Lithic clasts are predominately of granitic origin, giving the sands a distinct degraded batholithic-source appearance (a complete petrographic description of this unit can be found in Dragovich and others, 2011). Beds are warped and distorted, with measured attitudes striking 240 to 360° and dipping 0 to 15° (both north and south). Overall structure of the area suggests this might be a fold axis south of the Monroe fault. Although several models are possible, elevated Olympia beds on the SE highlands south of this site (for example, site 24D) might be a product of Quaternary uplift along the Monroe fault. Disseminated organic material collected at this site provided a radiocarbon age of 24,790±170 B.P. (See radiocarbon age sample 10-49E in Appendix 1.) Latitude/longitude of site is 47.845773/-121.873481. (See map sheet in Dragovich and others, 2011.)

Radiocarbon Age Site 50H, Photo 2150

Olympia beds (unit Qc_o), ancient Skykomish River-provenance alluvium, exposed along Woods Creek east of Monroe and less than a half mile upstream from Highway 2. Strata here consist of nonglacial micaceous sand, silt, silty clay, and pebbly sand with disseminated organic material including abundant carbonized plant debris, peat, and flattened sticks (some visible in the photo) in an eroded bank along the creek and about 20 ft above the ordinary high water mark (see petrographic description of unit in Dragovich and others, 2011). Beds are slightly tilted, with measured strikes between 50° and 162° and dips of 5° to 6°. Strata at this site are compositionally and stratigraphically similar to strata at nearby site 56A. Organics here were radiocarbon dated at 18,730 ± 110 yr B.P. (See radiocarbon age sample 10-50H in Appendix 1.) Latitude/longitude of site is 47.860855/-121.955319. (See map sheet in Dragovich and others, 2011.)

Site 51U, Photo 2161

Dark tuffs that are part of the 'volcanic rocks of Mount Persis' (unit Evt_{pd}) exposed at the Steffen farm on Ben Howard Road, south of the Skykomish River and on the very northern edge of the SE Highlands. This outcrop is at a waterfall. Vesicular andesite overlies a vitric gray tuff (in apparent conformity); both the contact and aligned vesicles are clearly visible and indicate a strike of 250° and dip of 15°. Blue pen near top center of photograph for scale. See Dragovich and others (2011) for a complete description of this unit. (See map sheet in Dragovich and others, 2011.)

Significant and Radiocarbon Age Site 56A, Photo 2228

An exposure of Olympia beds (unit Qc_o), nonglacial Skykomish River-provenance ancient alluvium, composed here of stratified micaceous sand, silt, and peat (visible in this photo) with minor gravel, well-exposed in a Woods Creek cutbank just a few hundred feet upstream from Highway 2 east of Monroe. Sand and silt is light yellow-brown, laminated, and crossbedded. Some bedding is deformed and distorted, probably as a result of liquefaction, and folded silt beds are evident, some containing carbonized wood. Sands composed of hornblende and plagioclase, with meta-argillite, volcanic, and granitic lithic grains. Some granitic lithic sand grains contain potassium feldspar and biotite, giving the impression that some of the source rocks are true granitics (a complete description of this unit can be found in Dragovich and others, 2011). Two radiocarbon dates were obtained from peat at this site: 19,920 ± 130 yr B.P. and 17,500 ± 80 yr B.P. The latter date is probably less reliable. (See notes for the two 10-56A radiocarbon age samples in Appendix 1.) Bedding was measured to strike and dip 140° and 5° respectively, but localized slumping may have altered the original attitude. Site is at latitude/longitude 47.858016/-121.957805. (See map sheet in Dragovich and others, 2011.)

Radiocarbon Age Site 56A, Photo 2235 (See also description above for Site 56A, Photo 2228)

Pre-Fraser continental deposits (unit Qc_{pf}) located just downriver from the site of photo 2228 above. Here, thin beds of fine and medium-grained sand and silt, some crossbedded, are distorted (as a result of liquefaction), with bedding locally chaotic and rootless folds evident in deformed silt. Undisturbed bedding strikes 59 to 75° and dips 14 to 16°. (See map sheet in Dragovich and others, 2011.)